# Carbon Monitoring System Flux Net Biosphere Exchange 2020 (CMS-Flux NBE 2020)

Junjie Liu[1,2*], Latha Baskaran[1], Kevin Bowman[1], David S. Schimel[1], A. Anthony Bloom[1], Nicholas C. Parazoo[1], Tomohiro Oda[3,4], Dustin Carroll[5], Dimitris Menemenlis[1], Joanna Joiner[6], Roisin Commane[7], Bruce Daube[8], Lucianna V. Gatti[9], Kathryn McKain[10,11], John Miller[10], Britton B. Stephens[12], Colm Sweeney[10], Steven Wofsy[8],

1. Jet Propulsion Laboratory, Caltech, CA
2. Caltech, CA
3. Global Modeling and Assimilation Office, NASA Goddard Space Flight Center
4. Goddard Earth Sciences Technology and Research, Universities Space Research Association, Columbia, MD
5. Moss Landing Marine Laboratories, San José State University, California, CA
6. Laboratory for Atmospheric Chemistry and Dynamics, NASA Goddard Space Flight Center
7. Lamont-Doherty Earth Observatory of Columbia University, NY
8. Harvard University, Cambridge, MA
9. LaGEE, CCST, INPE- National Institute for Space Researc, Brazil
10. NOAA, Global Monitoring Laboratory, Boulder, CO 80305
11. University of Colorado, Cooperative Institute for Research in Environmental Sciences, Boulder, CO
11. National Center for Atmospheric Research, Boulder, CO 80301

Correspondence: Junjie Liu (junjie.liu@jpl.nasa.gov)

**Abstract**. Here we present a global and regionally-resolved terrestrial net biosphere exchange (NBE) dataset with corresponding uncertainties between 2010–2018: CMS-Flux NBE 2020. It is estimated using the NASA Carbon Monitoring System Flux (CMS-Flux) top-down flux inversion system that assimilates column $CO_2$ observations from the Greenhouse gases Observing SATellite (GOSAT) and the NASA's Observing Carbon Observatory -2 (OCO-2). The regional monthly fluxes are readily accessible as tabular files, and the gridded fluxes are available in NetCDF format. The fluxes and their uncertainties are evaluated by extensively comparing the posterior $CO_2$ mole fractions with $CO_2$ observations from aircraft and the NOAA marine boundary layer reference sites. We describe the characteristics of the dataset as global total, regional climatological mean, and regional annual fluxes and seasonal cycles. We find that the global total fluxes of the dataset agree with atmospheric $CO_2$ growth observed by the surface-observation network within uncertainty. Averaged between 2010 and 2018, the tropical regions range from close-to neutral in tropical South America to a net source in Africa; these contrast with the extra-tropics, which are a net sink of 2.5 ± 0.3 gigaton carbon per year. The regional satellite-constrained NBE estimates provide a unique perspective for understanding the terrestrial biosphere carbon dynamics and monitoring changes in regional contributions to the changes of atmospheric $CO_2$ growth rate. The gridded and regional aggregated dataset can be accessed at: https://doi.org/10.25966/4v02-c391 (Liu et al., 2020).

## 1 Introduction

New "top-down" inversion frameworks that harness satellite observations provide an important complement to global aggregated fluxes (e.g., Global Carbon Project, Friedlingstein et al., 2019) and inversions based on surface $CO_2$ observations (e.g., Chevallier et al., 2010), especially over the tropics and the Southern Hemisphere (SH) where conventional surface $CO_2$ observations are sparse. The net biosphere exchange (NBE) is far more variable than ocean fluxes (Lovenduski and Bonan, 2017) or fossil fuel emissions (Yin et al, 2019), and is thus the focus of this dataset estimated from a top-down atmospheric $CO_2$ inversion of satellite column $CO_2$ dry-air mole fraction ($X_{CO2}$). Here, we present the global and regional NBE as a series of maps, time series and tables, and disseminate it as a public dataset for further analysis and comparison to other sources of flux information. The gridded NBE dataset and its uncertainty, air-sea fluxes, and fossil fuel emissions are also available, so that users can calculate carbon budget from regional to global scale. Finally, we provide a comprehensive evaluation of both mean and uncertainty estimates against the $CO_2$ observations from independent airborne datasets and the NOAA marine boundary layer (MBL) reference sites (Conway et al., 1994).

Global top-down atmospheric $CO_2$ flux inversions have been historically used to estimate regional terrestrial NBE, which is the net carbon flux of all the land-atmosphere exchange processes except fossil fuel emissions. They make uses of the spatiotemporal variability of atmospheric $CO_2$, which is dominated by NBE, to infer net carbon exchange at the surface (Chevallier et al., 2005; Baker et al., 2006; Liu et al., 2014). The accuracy of the NBE from top-down flux inversions is determined by the density and accuracy of the $CO_2$ observations, the accuracy of modeled atmospheric transport, and knowledge of the prior uncertainties of the flux inventories.

For $CO_2$ flux inversions based on high precision *in situ* and flask observations, the measurement error is low (<0.2 parts per million (ppm)) and not a significant source of error; however, these observations are limited spatially, and are concentrating primarily over North America (NA) and Europe (Crowell et al., 2019). Satellite $X_{CO2}$ from $CO_2$-dedicated satellites, such as the Greenhouse Gases Observing Satellite (GOSAT) (launched in July 2009) and the Observing Carbon Observatory 2 (OCO-2) (Crisp et al., 2017) have much broader spatial coverage (O'Dell et al., 2018), which fill the observational gaps of conventional surface $CO_2$ observations, but they have up to an order of magnitude higher single-sounding uncertainty and potential systematic errors compared to the *in situ* and flask $CO_2$ observations. Recent progress in instrument error characterization, spectroscopy, and retrieval methods have significantly improved the accuracy and precision of the $X_{CO2}$ retrievals (O'Dell et al., 2018; Kiel et al., 2019). The single sounding random error of $X_{CO2}$ from OCO-2 is ~1.0 ppm (Kulawik et al., 2019). A recent study by Byrne et al. (2020) shows less than a 0.5 ppm difference between posterior $X_{CO2}$ constrained by a recent data set, ACOS-GOSAT b7 $X_{CO2}$ retrievals, and those constrained by conventional surface $CO_2$ observations. Chevallier et al. (2019) also showed that an OCO-2 based flux inversion had similar performance to surface $CO_2$ based flux inversions when comparing posterior $CO_2$ mole fractions to aircraft $CO_2$ in the free troposphere. Results from these studies show that systematic uncertainties in $CO_2$ retrievals from satellites are comparable to, or smaller than, other uncertainty sources in atmospheric inversions (e.g. transport).

A newly-developed biogeochemical model-data fusion system, CARDAMOM, made progress in producing NBE uncertainties, along with mean values that are consistent with a variety of

observations assimilated through a Markov Chain Monte Carlo (MCMC) method (Bloom et al., 2016; 2020). Transport model errors in general have also been reduced relative to earlier transport model intercomparison efforts, such as TransCom 3 (Gurney et al., 2004; Gaubert et al., 2019). Advancements in satellite retrieval, transport, and prior terrestrial biosphere modeling have led to more mature inversions constrained by satellite $X_{CO2}$ observations.

Two satellites, GOSAT and OCO-2, have now produced more than 10 years of observations. Here we harness the CMS-Flux inversion framework (Liu et al., 2014; 2017; 2018; Bowman et al., 2017) to generate an NBE product: CMS-Flux NBE 2020, by assimilating both GOSAT and OCO-2 from 2010–2018. The dataset is the longest satellite-constrained NBE product so far. The CMS-Flux framework exploits globally available $X_{CO2}$ to infer spatially-resolved total surface-atmosphere exchange. In combination with constituent fluxes, e.g., Gross Primary Production (GPP), NBE from CMS-Flux framework have been used to assess the impacts of El Niño on terrestrial biosphere fluxes (Bowman et al, 2017; Liu et al, 2017) and the role of droughts in the North American carbon balance (Liu et al, 2018). These fluxes have furthermore been ingested into land-surface data assimilation systems to quantify heterotrophic respiration (Konings et al., 2019), evaluate structural and parametric uncertainty in carbon-climate models (Quetin et al., 2020), and inform climate dynamics (Bloom et al., 2020). We present the regional NBE and its uncertainty based on three types of regional masks: (1) latitude and continent, 2) distribution of biome types (defined by plant functional types) and continent, and 3) TransCom regions (Gurney et al., 2004).

The outline of the paper is as follows: Section 2 describes methods, and Sections 3 and 4 describe the dataset and the major NBE characteristics, respectively. We extensively evaluate the posterior

fluxes and uncertainties by comparing the posterior $CO_2$ mole fractions against aircraft observations and the NOAA MBL reference $CO_2$, and a gross primary production (GPP) product (section 5). In Section 6, we discuss the strength and weakness, and potential usage of the data. A summary is provided in Section 7, and Section 8 describes the dataset availability and future plan.

## 2 Methods

### 2.1 CMS-Flux inversion system

The CMS-Flux framework is summarized in Figure 1. The center of the system is the CMS-Flux inversion system, which optimizes NBE and air-sea net carbon exchanges with a 4D-Var inversion system (Liu et al., 2014). In the current system, we assume no uncertainty in fossil fuel emissions, which is a widely adopted assumption in global flux inversion systems (e.g., Crowell et al., 2019), since the uncertainty in fossil fuel emissions at regional scales is substantially less than the NBE uncertainties. The 4D-Var minimizes a cost function that includes two terms:

$$J(\mathbf{x}) = (\mathbf{x} - \mathbf{x}_b)^T \mathbf{B}^{-1} (\mathbf{x} - \mathbf{x}^b) + (\mathbf{y} - h(\mathbf{x}))^T \mathbf{R}^{-1} (\mathbf{y} - h(\mathbf{x})) \quad (1)$$

The first term measures the differences between the optimized fluxes and the prior fluxes normalized by the prior flux error covariance **B**. The second term measures the differences between observations ( $\mathbf{y}$ ) and the corresponding model simulations ( $h(\mathbf{x})$ ) normalized by the observation error covariance **R**. The term $h(\cdot)$ is the observation operator that calculates observation-equivalent model-simulated $X_{CO2}$. The 4D-Var uses the adjoint (i.e., the backward integration of the transport model) (Henze et al., 2004) of the GEOS-Chem transport model to calculate the sensitivity of the observations to surface fluxes. The configurations of the inversion system are summarized in Table 1. We run both the forward and adjoint at 4° x 5° spatial resolution, and optimize monthly NBE and air-sea carbon fluxes at each grid point from January 2010 to

December 2018. Inputs for the system include prior carbon fluxes, meteorological drivers, and the satellite $X_{CO2}$ (Figure 1). Section 2.2 (Table 2) describes the prior flux and its uncertainties, and section 2.3 (Table 3) describes the observations and the corresponding uncertainties.

### 2.2 The prior $CO_2$ fluxes and uncertainties

The prior $CO_2$ fluxes include NBE, air-sea carbon exchange, and fossil fuel emissions (see Table 2). The data sources for the prior fluxes are listed in Table 7 and provided in the gridded fluxes. Methods to generate prior ocean carbon fluxes and fossil fuel emissions are documented in Brix et al., (2015), Caroll et al. (2020), and Oda et al. (2018). The focus of this dataset is optimized terrestrial biosphere fluxes, so we briefly describe the prior terrestrial biosphere fluxes and its uncertainties.

We construct the NBE prior using the CARDAMOM framework (Bloom et al., 2016). CARDAMOM data assimilation system explicitly represents the time-resolved uncertainties in the NBE. The prior estimates are already constrained with multiple data streams accounting for measurement uncertainties following a similar Bayesian approach used in the 4D-variational approach. We use the CARDAMOM setup as described by Bloom et al. (2016, 2020) resolved at monthly timescales; data constraints include GOME-2 solar-induced fluorescence (Joiner et al., 2013), MODIS Leaf Area Index (LAI), and biomass and soil carbon (details on the data assimilation are provided in Bloom et al. (2020)). In addition, mean GPP and fire carbon emissions from 2010 - 2017 are constrained by FLUXCOM RS+METEO version 1 GPP (Tramontana et al., 2016; Jung et al., 2017) and GFEDv4.1s (Randerson et al., 2018), respectively, both assimilated with an uncertainty of 20%. We use the Olsen and Randerson (2001) approach to downscale

monthly GPP and respiration fluxes to 3-hourly timescales, based on ERA-interim re-analysis of global radiation and surface temperature. Fire fluxes are downscaled using the GFEDv4.1 daily and diurnal scale factors on monthly emissions (Giglio et al., 2013). Posterior CARDAMOM NBE estimates are then summarized as NBE mean and standard deviation values.

The NBE from CARDAMOM shows net carbon uptake of 2.3 GtC/year over the tropics and close to neutral in the extratropics (Figure S1). The year-to-year variability (i.e., interannual variability, IAV) estimated from CARDAMOM from 2010 –2017 is generally less than 0.1 $gC/m^2$/day outside of the tropics (Figure S1). Because of the weak interannual variability estimated by CARDAMOM, we use the same 2017 NBE prior for 2018.

CARDAMOM generates uncertainty along with the mean state. The relative uncertainty over the tropics is generally larger than 100%, and the magnitude is between 50% and 100% over the extra-tropics (Figure S2). We assume no correlation in the prior flux errors in either space or time. The temporal and spatial error correlation estimates can in principle be computed by CARDAMOM. We anticipate incorporating these error correlations in subsequent versions of this dataset.

### 2.3 Column $CO_2$ observations from GOSAT and OCO-2

We use the satellite-column $CO_2$ retrievals from Atmospheric Carbon Observations from Space (ACOS) team for both GOSAT (version 7.3) and OCO-2 (version 9) (Table 3). The use of the same retrieval algorithm and validation strategy adopted by the ACOS team to process both GOSAT and OCO-2 spectra maximizes the consistency between these two datasets. Both GOSAT and OCO-2 satellites carry high-resolution spectrometers optimized to return high precision measurements of reflected sunlight within $CO_2$ and $O_2$ absorption bands in the shortwave infrared

(Crisp et al., 2012). Both satellites fly in a sun-synchronous orbit. GOSAT has a 13:00 ± 0.15 hours local passing time and a three-day ground track repeat cycle. The footprint of GOSAT is ~10.5 km in diameter in sun-nadir view (Crisp et al., 2012). The daily number of soundings processed by the ACOS-GOSAT retrieval algorithm is between a few hundreds to ~2000. Further quality control and filtering reduce the ACOS-GOSAT $X_{CO2}$ retrievals to ~100 – 300 daily (Figure S5 in Liu et al., 2017). We only assimilate ACOS-GOSAT land nadir observations flagged as being good quality, which are the retrievals with quality flag equal to zero.

OCO-2 has a 13:30 local passing time and 16-day ground track repeat cycle. The nominal footprints of the OCO-2 are 1.25 km wide and ~2.4 km along the orbit. Because of their small footprints and sampling strategy, OCO-2 has many more $X_{CO2}$ retrievals than ACOS-GOSAT. To reduce the sampling error due to the resolution differences between the transport model and OCO-2 observations, we generate super observations by aggregating the observations within ~100 km (along the same orbit) (Liu et al., 2017). The super-obing strategy was first proposed in numerical weather prediction (NWP) to assimilate dense observations (Lorenc, 1981), and is still broadly used in NWP (e.g., Liu and Rabier, 2003). More detailed information about OCO-2 super observations can be found in Liu et al. (2017). OCO-2 has four observing modes: land nadir, land glint, ocean glint, and target. Following Liu et al. (2017), we only use land nadir observations. The super observations have more uniform spatial coverage and are more comparable to the spatial representation of ACOS-GOSAT observations and the transport model (see Figure S5 in Liu et al., 2017).

208 We directly use observational uncertainty provided with ACOS-GOSAT b7.3 to represent the
209 observation error statistics, **R**, in Eq 1. The uncertainty of the OCO-2 super observations is the
210 sum of the variability of $X_{CO2}$ used to generate each individual super observation and the mean
211 uncertainty provided in the original OCO-2 retrievals. Kulawik et al. (2019) showed that both
212 OCO-2 and ACOS-GOSAT bias-corrected retrievals have a mean bias of -0.1 ppm when compared
213 with $X_{CO2}$ from Total Carbon Column Observing Network (TCCON) (Wunch et al., 2011),
214 indicating consistency between ACOS-GOSAT and OCO-2 retrievals. O'Dell et al. (2018) showed
215 that the OCO-2 $X_{CO2}$ land nadir retrievals has RMS error of ~1.1 ppm when compared to TCCON
216 retrievals; the differences between OCO-2 $X_{CO2}$ retrievals and surface $CO_2$ constrained model
217 simulations are well within 1.0 ppm over most of the locations in the Northern Hemisphere (NH),
218 where most of the surface $CO_2$ observations are located.
219
220 The magnitude of observation errors used in **R** is generally above 1.0 ppm, larger than the sum of
221 random error and biases in the observations. The ACOS-GOSAT b7.3 observations from July
222 2009–June 2015 are used to optimize fluxes between 2010 and 2014, and the OCO-2 $X_{CO2}$
223 observations from Sep 2014–June 2019 are used to optimize fluxes between 2015 and 2018.
224
225 The observational coverage of ACOS-GOSAT and OCO-2 is spatiotemporally dependent, with
226 more coverage during summer than winter over the NH, and more observations over mid-latitudes
227 than over the tropics (Figure S3). The variability (i.e., standard deviation) of annual total number
228 of observations from 2010–2014 is within 4% of the annual mean number for ACOS-GOSAT.
229 Except for a data gap in 2017 caused by a malfunction of OCO-2 instrument, the variability of

annual total number of observations between 2015 and 2018 is within 8% of the annual mean number for OCO-2.

### 2.4 Uncertainty quantification

The posterior flux error covariance is the inverse Hessian, which incorporates the transport, measurement, and background errors at the 4D-Var solution (Eq. 13 in Bowman et al, 2017). Posterior flux uncertainty projected to regions can be estimated analytically based on the methods described in Fisher and Courtier (1995) and Meirink et al. (2008), using either flux singular vectors or flux increments obtained during the iterative optimization (e.g., Niwa and Fujii, 2020). In this study, we rely on a Monte Carlo approach to quantify posterior flux uncertainties following Chevallier et al. (2010) and Liu et al. (2014), which is simpler and widely used. In this approach, an ensemble of flux inversions is carried out with an ensemble of priors and simulated observations to sample the uncertainties of prior fluxes (i.e., **B** in eq. 1) and observations (**R** in Eq. 1), respectively. The magnitude of posterior flux uncertainties is a function of assumed uncertainties in prior fluxes and observations, as well as the density of observations. Since the density of GOSAT and OCO-2 observations are stable (section 2.3) within their respective data record, we characterize the posterior flux uncertainties for 2010 and 2015 only, and assume the flux uncertainties for 2011–2014 are the same as 2010 and flux uncertainties for 2016–2018 are the same as 2015.

### 2.5 Evaluation of posterior fluxes

Direct NBE estimates from flux towers only provide a spatial representation of roughly 1 – 3 kilometers (Running et al., 1999), not appropriate to evaluate regional NBE from top-down flux inversions. Thus, we use two methods to indirectly evaluate the posterior NBE and its uncertainties.

One is to compare annual NBE anomalies and seasonal cycle to a gross primary production (GPP) product. The other is to compare posterior $CO_2$ mole fractions to independent (i.e., not assimilated in the inversion) aircraft and the NOAA MBL reference observations. The second method has been broadly used to indirectly evaluate posterior fluxes from top-down flux inversions (e.g., Stephens et al., 2007; Liu and Bowman, 2016; Chevallier et al., 2019; Crowell et al., 2019). In addition to these two methods, we also compare the NBE seasonal cycles to three publicly available top-down NBE estimates that are constrained by surface $CO_2$ observations (Tables 3 and 7).

#### 2.5.1 Evaluation against independent gross primary production (GPP) product

NBE is a small residual difference between two large terms: total ecosystem respiration (TER) and GPP, plus fire. A positive NBE anomaly (i.e., less uptake from the atmosphere) has been shown to correspond to reduced GPP caused by climate anomalies (e.g., Bastos et al., 2018), and the magnitude of net uptake is proportional to GPP in most biomes observed by flux tower observations (e.g., Falk et al., 2008). Since NBE is related not only to GPP, the comparison to GPP only serves as a qualitative measure of the NBE quality. For example, we would expect that the posterior NBE seasonality to be anti-correlated with GPP in the temperate and high latitudes. In this study, we use FLUXSAT GPP (Joiner et al., 2018), which is an upscaled GPP product based on flux tower GPP observations and satellite-based geometry adjusted reflectance from the MODerate-resolution Imaging Spectroradiometer (MODIS) and solar-induced chlorophyll fluorescence observations from Global Ozone Monitoring Experiment – 2 (GOME-2) (Joiner et al., 2013). Joiner et al. (2018) show that the agreement between FLUXSAT-GPP and GPP from flux towers is better than other available upscaled GPP products.

#### 2.5.2 Evaluation against aircraft and the NOAA marine boundary layer (MBL) reference $CO_2$ observations

277 The aircraft observations used in this study include those published in OCO-2 MIP ObsPack
278 August 2019 (CarbonTracker team, 2019), which include regular vertical profiles from flask
279 samples collected on light aircraft by NOAA (Sweeney et al., 2015) and other laboratories, regular
280 (two to four weekly) vertical profiles from the Instituto de Pesquisas Espaciais (INPE) over
281 tropical South America (SA) (Gatti et al., 2014), and from the Atmospheric Tomography (ATom,
282 Wofsy et al., 2018), HIAPER Pole-to-Pole (HIPPO, Wofsy et al., 2011), and the $O_2/N_2$ Ratio and
283 $CO_2$ airborne Southern Ocean Study (ORCAS) (Stephens et al., 2017) aircraft campaigns (Table
284 3). Figure 2 shows the aircraft observation coverage and density between 2010 and 2018. Most of
285 the aircraft observations are concentrated over NA. ATom had four (1–4) campaigns between
286 August 2016 to May 2018, spanning four seasons over the Pacific and Atlantic Ocean. HIPPO had
287 five (1–5) campaigns over the Pacific, but only HIPPO 3–5 occurred between 2010 and 2011.
288 HIPPO 1–2 occurred in 2009. Based on the spatial distribution of aircraft observations, we divide
289 the comparison into nine regions: Alaska, mid-latitude NA, Europe, East Asia, South Asia, Africa,
290 Australia, Southern Ocean, and South America (Table 4 and Figure 2).
291
292 We calculate several quantities to evaluate the posterior fluxes and their uncertainty with aircraft
293 observations. One is the monthly mean differences between posterior and aircraft $CO_2$ mole
294 fractions. The second is the monthly root mean square errors (RMSE) over each of nine sub-
295 regions, which is defined as:

296 $$RMSE = \left(\frac{1}{n}\sum_{i=1}^{n}\left(y^{o}_{aircraft} - y^{b}_{aircraft}\right)_i^2\right)^{\frac{1}{2}} \quad (2)$$

297 where $y^{o}_{aircraft}$ is the $i^{th}$ aircraft observation, $y^{b}_{aircraft}$ is the corresponding posterior $CO_2$ mole
298 fraction sampled at the $i^{th}$ aircraft location, and $n$ is the number of aircraft observations over each
299 region. The RMSE is computed over the $n$ aircraft observations within one of the nine sub-regions.

The mean differences indicate the magnitude of the mean posterior $CO_2$ bias, while the RMSE includes both random and systematic errors in posterior $CO_2$. The bias and RMSE could be due to errors in posterior fluxes, transport, and initial $CO_2$ concentrations. When errors in transport and initial $CO_2$ concentrations are smaller than the errors in the posterior fluxes, the magnitude of biases and *RMSE* indicates the accuracy of the posterior fluxes.

To evaluate the magnitude of posterior flux uncertainty estimates, we compare *RMSE* against the standard deviation of ensemble simulated aircraft observations (equation 3) from the Monte Carlo method (*$RMSE_{MC}$)*. The quantity $RMSE_{MC}$ can be written as:

$$RMSE_{MC} = [\frac{1}{nens}\sum_{iens=1}^{nens}((y_{aircraft}^{b(MC)})_{iens} - \bar{y}_{aircraft}^{b(MC)})^2\ ]^{\frac{1}{2}} \quad (3)$$

The variable $(y_{aircraft}^{b(MC)})_{iens}$ is the $i^{\text{th}}$ ensemble member of simulated aircraft observations from Monte Carlo ensemble simulations, $\bar{y}_{aircraft}^{b(MC)}$ is the mean, and *nens* is the total number of ensemble members. For simplicity, in equation (3), we drop the indices for the aircraft observations used in equation (2). In the absence of errors in transport and initial $CO_2$ concentrations, when the estimated posterior flux uncertainty reflects the "*true*" posterior flux uncertainty, we show in the *Appendix* that:

$$RMSE^2 = R_{aircraft} + {RMSE_{MC}}^2 \quad (4)$$

where $R_{aircraft}$ is the aircraft observation error variance, which could be neglected on regional scale.

We further calculate the ratio *r* between *RMSE* and $RMSE_{MC}$:

$$r = \frac{RMSE}{RMSE_{MC}} \quad (5)$$

A ratio close to one indicates that the posterior flux uncertainty reflects the true uncertainty in the posterior fluxes when the transport errors are small.

The presence of transport errors will make the comparison between *RMSE* and $RMSE_{MC}$ potentially difficult to interpret. Even when $RMSE_{MC}$ represents the actual uncertainty in posterior fluxes, the *RMSE* could be larger than $RMSE_{MC}$, since the differences between aircraft observations and model simulated posterior mole fractions *RMSE* could be due to errors in both transport and the posterior fluxes, while $RMSE_{MC}$ only reflects the impact of posterior flux uncertainty on simulated aircraft observations. In this study, we assume the primary sources of *RMSE* come from errors in posterior fluxes.

The *RMSE* and $RMSE_{MC}$ comparison only shows differences in $CO_2$ space. We further calculate the sensitivity of the *RMSE* to the posterior flux using the GEOS-Chem adjoint. We first define a cost function *J* as:

$$J = RMSE^2 \quad (6)$$

The sensitivity of the mean-square error to a flux, *x*, at location *i* and month *j* is

$$w_{i,j} = \frac{\partial J}{\partial x_{i,j}} \times x_{i,j} \quad (7)$$

This sensitivity is normalized by the flux magnitude. Equation 7 can be interpreted as the sensitivity of the $RMSE^2$ to a fractional change in the fluxes. We can estimate the time-integrated magnitude of the sensitivity over the entire assimilation window by calculating:

$$S_i = \frac{\sum_{j=1}^{M} |w_{i,j}|}{\sum_{k=1}^{P} \sum_{j=1}^{M} |w_{k,j}|} \quad (8)$$

where $P$ is the total number of grid points and $M$ is the total number of months from the time of the aircraft data to the beginning of the inversion. The numerator of equation (8) quantifies the absolute total sensitivity of the $RMSE^2$ to the fluxes at the $i^{th}$ grid. Normalized by the total absolute sensitivity across the globe, the quantity $S_i$ indicates the relative sensitivity of $RMSE^2$ to fluxes at the $i^{th}$ grid point. Note that $S_i$ is unitless, and it only quantifies sensitivity, not the contribution of fluxes at each grid to $RMSE^2$.

We use the NOAA MBL reference dataset (Table 7) to evaluate the $CO_2$ seasonal cycle over four latitude bands: 90ºN-60ºN, 60ºN-20ºN, 20ºN-20ºS, and 20ºS-90ºS. The MBL reference is based on a subset of sites from the NOAA Cooperative Global Air Sampling Network. Only measurements that are representative of a large volume air over a broad region are considered. In the comparison, we first remove the global mean $CO_2$ (https://www.esrl.noaa.gov/gmd/ccgg/trends/global.html ) from both the NOAA MBL reference and the posterior $CO_2$.

**2.6 Regional masks**

We provide posterior NBE from 2010 – 2018 using three sets of regional masks (Figure 3), in addition to the gridded product. The regional mask in Figure 3A is based on a combination of seven plant function types condensed from MODIS IGBP and the TransCom -3 regions (Gurney et al., 2004), which is referred as Region Mask 1 (RM1) in later description. There are 28 regions in Figure 3A: six in NA, four in SA, five in Eurasia (north of 40˚N), three in tropical Asia, three in Australia, and seven in Africa. The regional mask in Figure 3B is based on latitude and

365 continents with 13 regions in total, which is referred as Region Mask 2 (RM2) in later description.
366 Figure 3C is the TransCom regional mask with 11 regions on land.
367
368 **3 Dataset description**
369
370 We present the fluxes as globally, latitudinally, and regionally aggregated time series. We show
371 the nine-year average fluxes aggregated into RM1, RM2, and TransCom regions (Figure 3). The
372 aggregations are geographic (latitude and continent) and bio-climatic (biome by continent). For
373 each region in the geographic and biome aggregations, we show nine-year mean annual net fluxes
374 and uncertainties, and then the annual fluxes for each region as a set of time-series plots. The
375 month-by-month fluxes and uncertainties are available in tabular format, so the actual aggregated
376 fluxes may be readily compared to bottom-up extrapolated fluxes and Earth System models. Users
377 can also aggregate the gridded fluxes and uncertainties based on their own defined regional masks.
378 Table 5 provides a complete list of all data products available in the dataset. In section 4, we
379 describe the major characteristics of the dataset.
380 **4 Characteristics of the dataset**
381 **4.1 Global fluxes**
382 The annual atmospheric $CO_2$ growth rate, which is the sum of fossil fuel emissions and total annual
383 sink over land and ocean, is well-observed by the NOAA surface $CO_2$ observing network
384 (https://www.esrl.noaa.gov/gmd/ccgg/ggrn.php). We compare the global total flux estimates constrained
385 by GOSAT and OCO-2 with the NOAA $CO_2$ growth rate from 2010–2018, and discuss the mean
386 carbon sink over land and ocean. Over these nine years, the satellite-constrained atmospheric $CO_2$
387 growth rate agrees with the NOAA observed $CO_2$ growth rate within the uncertainty of the
388 posterior fluxes (Figure 4). The mean annual global surface $CO_2$ fluxes (in Gt C/yr) are derived

from the NOAA observed $CO_2$ growth rate (in ppm/yr) using a conversion factor of 2.124 GtC/ppm (Le Quéré et al., 2018). The estimated growth rate has the largest discrepancy with the NOAA observed growth rate in 2014, which may be due to a failure of one of the two solar paddles of GOSAT in May 2014 (Kuze et al., 2016). Over the nine years, the estimated total accumulated carbon in the atmosphere is 41.5 ± 2.4 GtC, which is slightly lower than the accumulated carbon based on the NOAA $CO_2$ growth rate (45.2 ± 0.4 GtC). On average, the land sink is 20 ± 8% of fossil fuel emissions, and the ocean sink is 30 ± 1% of fossil fuel emissions (Figure 4). These numbers are within the ranges of the corresponding estimates from GCP 2019 (Freidlingstein et al., 2019). The mean NBE and ocean sink from GCP 2019 are 21 ± 10% (~1.0 GtC estimated residual NBE uncertainty) and 26 ± 5% (~0.5 GtC estimated ocean flux uncertainty) of fossil fuel emissions respectively between 2010–2018. The GCP NBE here is calculated as the residual differences between fossil fuel, ocean fluxes, and atmospheric $CO_2$ growth rate, and it is also equivalent to the sum of carbon fluxes from land use changes, land sink, and residual balance reported by GCP. Over these nine years, we estimate that the land sink ranges from 37% of fossil fuel emissions in 2011 (a La Niña year) to only 5% in 2015 (an El Niño year), consistent with the range estimated by GCP of 35% in 2011 to 7% in 2015. We estimate that the ocean sinks range from 39% in 2015 to 23% of fossil fuel emissions in 2012, larger than the GCP estimated ocean flux ranges of 25% to 28% of fossil fuel emissions (Freidlingstein et al., 2019).

**4.2 Mean regional fluxes and uncertainties**

Figure 5 shows the nine-year mean regional annual fluxes, uncertainty, and its variability between 2010–2018. Table 6 shows an example of the dataset corresponding to Figure 5 A, D, and G. It shows that large net carbon uptake occurs over Eurasia, NA, and the Southern Hemisphere (SH) mid-latitudes. The largest net carbon uptake is over the eastern US (-0.4 ± 0.1 GtC (1σ uncertainty))

412 and high latitude Eurasia (-0.5 ± 0.1 GtC) (Figure 5A, B). We estimate a net land carbon sink of
413 2.5 ± 0.3 GtC/year between 2010–2013 over the NH mid to high latitudes, which agrees with 2.4
414 ± 0.6 GtC estimates over the same time periods based on a two-box model (Ciais et al., 2019). Net
415 uptake in the tropics ranges from close-to-neutral in tropical South America (0.1 ± 0.1 GtC) to a
416 net source in northern Africa (0.6 ± 0.2 GtC) (Figure 5A, B). The tropics exhibit both large
417 uncertainty and large variability. The NBE interannual variability over northern Africa and tropical
418 SA are 0.5 GtC and 0.3 GtC respectively, larger than the 0.2 GtC and 0.1 GtC uncertainty (Figure
419 5D, E). We also find collocation of regions with large NBE and GPP interannual variability (Figure
420 S4). The availability of flux estimates over the broadly used TransCom regions make it easy to
421 compare to previous studies. For example, we estimate that the annual net carbon uptake over
422 North America is 0.7 ± 0.1 GtC/year with 0.2 GtC variability between 2010 and 2018, which
423 agrees with 0.7 ± 0.5 GtC/year estimates based on surface $CO_2$ observations between 1996-2007
424 (Peylin et al., 2013).
425
426 **4.3 Interannual variabilities and uncertainties**
427 Here we present hemispheric and regional NBE interannual variabilities and corresponding
428 uncertainties (Figures 6 and 7, and corresponding tabular data files). In Figure 6, we further divide
429 the globe into three large latitude bands: tropics (20°S–20°N), NH extra-tropics (20°N–85°N), and
430 SH extra-tropics (60°S–20°S). The tropical NBE contributes 90% to the global NBE interannual
431 variability (IAV). The IAV of NBE over the extra-tropics is only about one-third of that over the
432 tropics. The dominant role of tropical NBE in the global IAV of NBE agrees with Figure 4 in
433 Sellers et al. (2018). The top-down global annual NBE anomaly is within the 1.0 GtC/yr

uncertainty of residual NBE (i.e., fossil fuel – atmospheric growth – ocean sink) calculated from GCP-2019 (Friedlinston et al., 2019) (Figure 6).

Figure 7 shows the annual NBE anomalies and uncertainties over a few selected regions based on RM1. Positive NBE indicates reduced net uptake relative to the 2010–2018 mean, and vice versa. Also shown in Figure 7 are GPP anomalies estimated from FLUXSAT. Positive GPP indicates increased productivity, and vice versa. GPP drives NBE in years where anomalies are inversely correlated (e.g., positive NBE and negative GPP), and TER drives NBE in years where anomalies of GPP and NBE have the same sign or are weakly correlated. Over tropical SA evergreen broadleaf forest, the largest positive NBE anomalies occur during the 2015–2016 El Niño, corresponding to large reductions in productively, consistent with Liu et al. (2017). In 2017, the region sees increased net uptake and increased productivity, implying a recovery from the 2015–2016 El Niño event. The variability in GPP explains 80% of NBE variability over this region over the nine-year period. In Australian shrubland, our inversion captures the increased net uptake in 2010 and 2011 due to increased precipitation (Poulter et al., 2014) and increased productivity. The variability in GPP explains 70% of the interannual variability in NBE. Over tropical south America savanna, the NBE interannual variability also shows strong negative correlations with GPP, with GPP explaining 40% of NBE interannual variability. Over the mid-latitude regions where the IAV is small, the $R^2$ between GPP and NBE is also small (0.0–0.5) as expected. But the increased net uptake generally corresponds to increased productivity. We also do not expect perfect negative correlation between NBE anomalies and GPP anomalies, as discussed in section 2.5. The comparison between NBE and GPP provides insight into when and where net fluxes are likely dominated by productivity.

### 4.4 Seasonal cycle

We provide the regional mean NBE seasonal cycle, its variability, and uncertainty based on the three regional masks (Table 5). Here we briefly describe the characteristics of the NBE seasonal cycle over the 11 TransCom regions, and its comparison to three independent top-down inversion results based on surface $CO_2$, which are CT-Europe (e.g., van der Laan-Luijkx et al., 2017) CAMS (Chevallier et al., 2005), and Jena CarbonScope (Rödenbeck et al., 2003). CMS-Flux-NBE differs the most from surface-$CO_2$ based inversions over the South American Tropical, Northern Africa, tropical Asia, and NH boreal regions. The CMS-Flux NBE has a larger seasonal cycle amplitude over tropical Asia and Northern Africa, where the surface $CO_2$ constraint is weak, while it has a smaller seasonal cycle amplitude over the boreal region; this may be due to the sparse satellite observations over the high latitudes and weaker seasonal amplitude of the prior CARDAMOM fluxes. The comparison to FluxSat GPP can only qualitatively evaluate the NBE seasonal cycle, but cannot differentiate among different estimates. In general, the months that have larger productivity corresponds to months with a net uptake of carbon from the atmosphere, especially over the NH (Figure 8). More research is still needed to understand the seasonal cycles of NBE, including its phase (i.e., transition from source to sink) and amplitude (peak-to-trough difference), and its relationships with GPP and respiration.

## 5 Evaluation against independent aircraft $CO_2$ observations

### 5.1 Comparison to aircraft observations over nine sub-regions

In this section, we evaluate posterior $CO_2$ against aircraft observations over the nine sub-regions listed in Table 4 and Figure 2. We compare the posterior $CO_2$ to aircraft $CO_2$ mole fractions above

480 the planetary boundary layer and up to mid troposphere (1–5 km) at the locations and time of
481 aircraft observations, and then calculate the monthly mean error statistics between 1–5 km. The
482 aircraft observations between 1–5 km are more sensitive to regional fluxes (Liu et al., 2015; Liu
483 and Bowman, 2016). Scatter plots in the left column of Figure 9 show regional monthly mean de-
484 trended aircraft $CO_2$ observations (x-axis) versus the simulated detrended posterior $CO_2$ (y-axis).
485 We used the NOAA global $CO_2$ trend to detrend both the observations and model simulated mole
486 fractions (ftp://aftp.cmdl.noaa.gov/products/trends/co2/co2_trend_gl.txt). Over the NH regions (A,
487 B, C, D) and Africa (F), the $R^2$ is greater than or equal to 0.9, which indicates that the posterior
488 $CO_2$ captures the observed seasonality. The low $R^2$ (0.7) value in South Asia is caused by one
489 outlier. Over the Southern Ocean, Australia, and SA, the $R^2$ is between 0.2 and 0.4, reflecting
490 weaker $CO_2$ seasonality over these regions and possible bias in ocean flux estimates (see
491 discussions later).
492
493 The right panel of Figure 9 shows the monthly mean differences between posterior $CO_2$ and aircraft
494 observations (black), *RMSE* (equation 2) (blue line), and $RMSE_{MC}$ (equation 3) (red line). The
495 magnitude of the mean differences between the posterior $CO_2$ and aircraft observations is less than
496 0.5 ppm except over the Southern Ocean, which has a -0.8 ppm bias. The mean differences between
497 posterior $CO_2$ and aircraft observations are primarily caused by errors in transport and biases in
498 assimilated satellite observations, while $RMSE_{MC}$ is 'internal flux error' projected into mole
499 fraction space. With the exception of the Southern Ocean, for all regions mean bias is significantly
500 less than $RMSE_{MC}$, which suggests that transport and data bias in satellite observations may be
501 much smaller than the internal flux errors. Note that $RMSE_{MC}$ is smaller than *RMSE* over the first

~six months of simulation, which may indicate a dominant impact of errors in transport and initial $CO_2$ concentration on posterior $CO_2$ *RMSE*.

As demonstrated in section 2.5, comparing *RMSE* and $RMSE_{MC}$ is a test of the accuracy of posterior flux uncertainty estimate. Over all the regions, the differences between *RMSE* and $RMSE_{MC}$ are smaller than 0.3 ppm, which indicates a comparable magnitude between empirical posterior flux uncertainty estimates from the Monte Carlo method and the actual posterior flux uncertainty over the regions that these aircraft observations are sensitive to. These aircraft observations are sensitive to fluxes over a broad region as shown in Figure S5.

### 5.2 Comparison to aircraft observations from ATom and HIPPO aircraft campaigns

Figures 10 and 11 show comparisons to aircraft $CO_2$ from ATom 1–4 campaigns spanning four seasons, and HIPPO 3–5 over the Pacific Ocean between 1–5 km. The vertical curtain comparisons are shown in Figure S6 and S7. The mean differences between posterior $CO_2$ and aircraft $CO_2$ are quite uniform (within 0.5 ppm) throughout the column except over the Atlantic Ocean during ATom 1–2 and the Southern Ocean during ATom 1 (Figures S6 and S7). Also shown in Figures 10 and 11 are *RMSE* of each aircraft campaign (middle column) and the ratio between *RMSE* and $RMSE_{MC}$ (right column). A ratio larger than one between *RMSE* and $RMSE_{MC}$ indicates errors in either transport or underestimation of the posterior flux uncertainty (section 2.5).

Over most of the flight tracks during ATom 1–4, the posterior $CO_2$ errors are between -0.5 and 0.5 ppm, the *RMSE* is smaller than 0.5 ppm, and the ratio between *RMSE* and $RMSE_{MC}$ is smaller than or equal to 1. However, off the coast of Africa during ATOM -1 and -2 and over the Southern

Ocean during ATOM-1, the mean differences between posterior $CO_2$ and aircraft observations are larger than 0.5 ppm. During ATOM-1 (29 July – 23 Aug 2016), the mean differences between posterior $CO_2$ and aircraft $CO_2$ show large negative biases, while during ATOM-2 (26 Jan 2017–21 Feb 2017), it has large positive biases off the coast of Africa. The ratio between *RMSE* and $RMSE_{MC}$ is significantly larger than one over these regions, which indicates an underestimation of posterior flux uncertainty or large magnitude of transport errors during that time period.

We further run adjoint sensitivity analyses over the three regions with ratios significantly larger than one to identify the posterior fluxes that could contribute to the large differences between posterior $CO_2$ and aircraft observations during ATOM 1–2. We run the adjoint model backward for three months from the observation time and calculate $S_i$ as defined in equation (7). The adjoint sensitivity analysis indicates that the large mismatch between aircraft observations and model simulations during ATOM-1 and -2 off the coast of Africa could be potentially driven by errors in posterior fluxes over tropical Africa (Figure S8). The large posterior $CO_2$ errors and large ratio between *RMSE* and $RMSE_{MC}$ over the Southern Ocean during ATOM-1 are driven by flux errors in oceanic fluxes around 30°S and over Australia (Figure S9), which also contribute to the large errors in comparison to aircraft observations over the Southern Ocean shown in Figure 9 H.

During the HIPPO aircraft campaigns, the absolute errors in posterior $CO_2$ across the Pacific are less than 0.5 ppm except over the Arctic Ocean and over Alaska in summer (Figure 11), consistent with Figure 10A. The large errors over the Arctic Ocean may be related to both transport errors and the accuracy of high latitude fluxes. Byrne et al. (2020) provide a brief summary of the

challenges in simulating $CO_2$ over high latitudes using a transport model with 4° x 5° resolution. Increasing the resolution of the transport model may reduce transport errors over high latitudes.

We run adjoint sensitivity analysis over the high-latitude regions where the differences between posterior $CO_2$ and aircraft observations are large (Figure 11). The adjoint sensitivity analysis (Figure S10) shows that the large errors over these regions could be driven by errors in fluxes over Alaska as well as broad NH mid-latitude regions.

### 5.3 Comparison to MBL reference sites

Since MBL reference sites sample air over broad regions, the comparison to detrended MBL observations indirectly evaluates the NBE over large regions. Figure 12 shows the comparison over four latitude bands. The uncertainty of posterior $CO_2$ concentration is from the MC method. Except over 90°S-20°S, the differences between observations and posterior $CO_2$ are within posterior $CO_2$ uncertainty estimates. Over 90°S-20°S, the posterior $CO_2$ has positive bias in 2013 and 2014 and negative bias and much weaker seasonality between Jan 2015 – Dec 2018 compared to observations, which indicates possible biases in Southern Ocean flux estimates. The low bias over Southern Ocean is consistent with aircraft comparison during OCO-2 period (Figures 9 and 10). The posterior $CO_2$ have smallest bias and random errors over the tropical latitude band. The $R^2$ is above 0.9 over NH mid to high latitudes, consistent with Figure 9.

## 6 Discussion

Evaluation of posterior flux uncertainty estimates by comparing posterior $CO_2$ error statistics (*RMSE,* Equation 2) with the standard deviation of ensemble simulated $CO_2$ from Monte Carlo uncertainty quantification method ($RMSE_{MC}$, equation 3) has its limitations. A comparable *RMSE*

571 and $RMSE_{MC}$ indicates a small magnitude of transport errors and reasonable posterior uncertainty
572 estimates. A much larger *RMSE* than $RMSE_{MC}$ could be due to errors in either transport or
573 underestimation of the posterior flux uncertainty or both. The presence of transport errors makes
574 the interpretation of the *RMSE* and $RMSE_{MC}$ complex. A better, independent quantification of
575 transport errors is needed in the future in order to rigorously use the comparison statistics between
576 aircraft observations and posterior $CO_2$ to diagnose flux errors.
577
578 Comparison to aircraft observations shows regionally-dependent accuracy in posterior fluxes.
579 ATom observations show seasonally-dependent biases over the Atlantic, implying possible
580 seasonally dependent errors in posterior fluxes over northern to central Africa. Therefore, we
581 recommend combining NBE with other ancillary variables, e.g., GPP, to better understand carbon
582 dynamics. Combining NBE with component carbon fluxes can shed light on the processes
583 controlling the changes of NBE (e.g., Bowman et al, 2017; Liu et al., 2017). NBE can be written
584 as:
585 NBE= TER + fire - GPP (8)
586 where TER is total ecosystem respiration (TER) (Figure 1). Satellite carbon monoxide (CO)
587 observations provide constraints on fire emissions (Arellano et al, 2006, van der Werf, 2008; Jones
588 et al, 2009; Jiang et al., 2015, Bowman et al, 2017; Liu et al., 2017). In addition to the FLUXSAT-
589 GPP product used here, solar induced chlorophyll fluorescence (SIF) can be directly used as a
590 proxy for GPP (e.g., Parazoo et al, 2014). Once NBE, fire, and GPP carbon fluxes are quantified,
591 TER can be calculated as a residual (e.g., Bowman et al, 2017; Liu et al., 2017, 2018).
592

Because of the diffusive manner of atmospheric transport and the limited observation coverage, the gridded flux values are not independent from each other. The errors and uncertainties of the fluxes at each individual grid point are larger than regional aggregated fluxes. Interpreting NBE at each individual grid point requires caution. But at the same time, satellite $CO_2$ constrained NBE can potentially resolve fluxes at spatial scales smaller than the traditional TransCom regions. Here, we provide regional fluxes at two predefined regions in addition to TransCom. We encourage data users to use the data at propriate regional scales.

The variability and changes are more robust than the mean NBE fluxes from top-down flux inversions in general (Baker et al., 2006b). The errors in transport and potential biases in observations are mostly stable in time, so biases in the mean fluxes tend to cancel out when computing interannual variability and year-to-year changes (Schuh et al., 2019; Crowell et al., 2019).

The global fossil fuel emissions have ~5% uncertainty (GCP, 2019). However, they are regionally inhomogeneous. We neglect the uncertainties in fossil fuel emissions, which will introduce additional error in regions of rapid fossil fuel growth or in areas with noisier statistics (Yin et al., 2019). In the future, we will account for uncertainties in fossil fuel emissions.

The posterior NBE includes all types of land fluxes except fossil fuel emissions, which is equivalent to the sum of land use change fluxes and land sinks published by the GCP. The sum of regional NBE and fossil fuel emissions is an index of the contribution of any specific region to the changes of the atmospheric $CO_2$ growth rate. Even over the continental US, where fossil fuel

emissions are ~1.5 GtC/year, the changes of regional NBE can significantly modify contributions to the changes of atmospheric $CO_2$ (Liu et al., 2018). Since NBE has high variability and its predicted changes in the future are likely to have large uncertainties, quantifying regional NBE is critical to monitoring regional contributions to atmospheric $CO_2$ growth rate, and ultimately to guide mitigation to limit warming to 1.5°C above pre-industrial levels (IPCC, AR6).

## 7 Summary

Terrestrial biosphere carbon fluxes are the largest contributor to the interannual variability of the atmospheric $CO_2$ growth rate. Therefore, monitoring its change at regional scales is essential for understanding how it responds to $CO_2$, climate and land use. Here, we present the longest terrestrial flux estimates and their uncertainties constrained by $X_{CO2}$ from 2010–2018 on self-consistent global and regional scales (CMS-Flux NBE 2020). We qualitatively evaluate the net flux estimates by comparing its variability with GPP variability, and provide comprehensive evaluation of posterior fluxes and the uncertainties by comparing posterior $CO_2$ with independent $CO_2$ observations from aircraft and the NOAA MBL reference sites. The estimated posterior flux uncertainty agrees with the expected uncertainty in the posterior fluxes based on the comparison to aircraft $CO_2$ observations. This dataset can be used in understanding controls on regional NBE interannual variability, evaluating biogeochemical models, and supporting the monitoring of regional contributions to changes in atmospheric $CO_2$.

## 8 Data availability and future update

The CMS-Flux NBE 2020 data are available at: https://doi.org/10.25966/4v02-c391 (Liu et al., 2020). The regional aggregated fluxes are provided as *csv* files with file size ~10MB, and the

639 gridded data is provided in NetCDF format with file size ~1.4 GB. The full ensemble of posterior
640 fluxes used to estimate posterior flux uncertainties are provided in NetCDF format with file size
641 ~30MB. Table 7 lists the sources of the data used in producing and evaluating the CMS-Flux NBE
642 2020 data product.
643
644 The quality of $X_{CO2}$ from satellite observations is continually improving. The OCO-2 v10 $X_{CO2}$
645 has been released in June 2020 along with the full GOSAT record (June 2009–Jan 2020) processed
646 by the same retrieval algorithm as OCO-2. Continuing to improving the quality of satellite
647 observations and extending the NBE estimates beyond 2018 in the future will help us better
648 understand interactions between terrestrial biosphere carbon cycle and climate and provide support
649 in monitoring the regional contributions to the changes of atmospheric $CO_2$. Thus, we plan a future
650 update of the dataset on an annual basis, with a goal to support current scientific research and
651 policy making.

652 **9 Author contributions**

653 JL designed the study and led the writing of the paper in close collaboration with KB and DS. LB
654 helped generate the plots and created all the data files. AAB provided the prior of the terrestrial
655 biosphere carbon fluxes. NP helped interpret the GPP evaluation. DM and DC generated the prior
656 ocean carbon fluxes. TO generated the ODIAC fossil fuel emissions. JJ provided the FLUXSAT
657 GPP product. BD and SW provided and contributed to the interpretation of HIPPO aircraft $CO_2$
658 observation comparisons. BS, KM, and CS provided ORCAS aircraft $CO_2$ observations and
659 contributed interpretation of aircraft $CO_2$ observation comparisons. LVG and JM provided INPE
660 aircraft $CO_2$ observations and contributed interpretation of aircraft $CO_2$ observation comparisons.
661 CS and KM provided ATom and the NOAA aircraft CO2 observations and contributed

interpretation of aircraft $CO_2$ observation comparisons. We furthermore acknowledge funding from the EU for the ERC project "ASICA" (grant number 649087) to Wouter Peters (Groningen University) and EU and NERC (UK) funding to Emanuel Gloor (University of Leeds), which contributed to the INPE Amazon greenhouse sampling program. All authors contributed to the writing, and have reviewed and approved the paper.

## 10 Competing interest

The authors declare that they have no conflict of interest.


## Acknowledgement

Resources supporting this work were provided by the NASA High-End Computing (HEC) Program through the NASA Advanced Supercomputing (NAS) division at Ames Research Center. We acknowledge the funding support from NASA OCO-2/3 Science Team, Carbon Monitoring System (CMS), and Making Earth Science Data Records for Use in Research Environments (MEaSUREs) programs. Tomohiro Oda is supported by the NASA Carbon Cycle Science program (grant no. NNX14AM76G). We acknowledge EU and NERC (UK) funding to Emanuel Gloor, University of Leeds which substantially contributed to the INPE Amazon greenhouse sampling program. CarbonTracker Europe results provided by Wageningen University in collaboration with the ObsPack partners (http://www.carbontracker.eu). Part of the research was carried out at Jet Propulsion Laboratory, Caltech.


## Appendix

As shown in Kalnay (2003):

$$RMSE^2 = R_{aircraft} + HP^a H^T \quad \text{(A.1)}$$

where $R_{aircraft}$ is the aircraft observation error variance, and $P^a$ is the posterior flux error covariance. The $H$ is linearized observation operator, which transfers posterior flux errors to aircraft observation space, and $H^T$ is its adjoint. In the Monte Carlo method, the posterior flux error covariance $P^a$ is approximated by:

$$P^a = \frac{1}{nens} X^a X^{aT} \quad \text{(A.2)}$$

where $X^a$ is the ensemble perturbations written as:

$$X^a = x^a - \bar{x}^a \quad \text{(A.3)}$$

where $x^a$ is the ensemble posterior fluxes from Monte Carlo, and $\bar{x}^a$ is the mean.

Therefore, $HP^aH^T$ can be written as:

$$HP^aH^T = \frac{1}{nens}[h(x^a) - h(\bar{x}^a)][h(x^a) - h(\bar{x}^a)]^T \quad \text{(A.4)}$$

The right hand side is the same as the definiation of $RMSE_{MC}$ in the main text.

Therefore, when the posterior flux uncertainty estimated by Monte Carlo method represents the actual uncertainty in posterior fluxes, equation (A.1) can be written as:

$$RMSE^2 = R_{aircraft} + RMSE_{MC}^2 \quad \text{(A.5)}.$$

It is the same as equation (3) in the main text.

References

Arellano Jr, A.F., Kasibhatla, P.S., Giglio, L., Van der Werf, G.R., Randerson, J.T., and Collatz, G.J.: Time-dependent inversion estimates of global biomass-burning CO emissions using Measurement of Pollution in the Troposphere (MOPITT) measurements, J. Geophys. Res: Atmos., 111, D09303, https://doi.org/10.1029/2005JD006613, 2006.

Baker, D.F., Doney, S.C., and Schimel, D.S.: Variational data assimilation for atmospheric CO2, Tellus B: Chem. Phys. Meteorol., 58, 359-365, https://doi.org/10.1111/j.1600-0889.2006.00218.x, 2006a.

Baker, D.F., Law, R.M., Gurney, K.R., Rayner, P., Peylin, P., Denning, A.S., Bousquet, P., Bruhwiler, L., Chen, Y.H., Ciais, P., and Fung, I.Y.: TransCom 3 inversion intercomparison: Impact of transport model errors on the interannual variability of regional CO2 fluxes, 1988–2003, Global Biogeochem. Cy., 20, GB1002, https://doi.org/10.1029/2004GB002439, 2006b.

Bastos, A., Friedlingstein, P., Sitch, S., Chen, C., Mialon, A., Wigneron, J.-P., Arora, V. K., Briggs, P. R., Canadell, J. G., and Ciais, P.: Impact of the 2015/2016 El Niño on the terrestrial carbon cycle constrained by bottom-up and top-down approaches. Philos. Trans. R Soc. Lond. B. Biol. Sci., 373, 1760, https://doi.org/10.1098/rstb.2017.0304, 2018.

Bloom, A.A., Exbrayat, J.F., van der Velde, I.R., Feng, L., and Williams, M.: The decadal state of the terrestrial carbon cycle: Global retrievals of terrestrial carbon allocation, pools, and residence times. Proc. Natl Acad. Sci., 113, 1285-1290, 2016.

Bloom, A. A., Bowman, K. W., Liu, J., Konings, A. G., Worden, J. R., Parazoo, N. C., Meyer, V., Reager, J. T., Worden, H. M., Jiang, Z., Quetin, G. R., Smallman, T. L., Exbrayat, J.-F., Yin, Y., Saatchi, S. S., Williams, M., and Schimel, D. S.: Lagged effects dominate the inter-annual variability of the 2010–2015 tropical carbon balance, Biogeosciences Discuss., https://doi.org/10.5194/bg-2019-459, in review, 2020.

Bowman, K.W., Liu, J., Bloom, A.A., Parazoo, N.C., Lee, M., Jiang, Z., Menemenlis, D., Gierach, M.M., Collatz, G.J., Gurney, K.R., and Wunch, D.: Global and Brazilian carbon response to El Niño Modoki 2011–2010, Earth Space Sci., 4, 637-660, https://doi.org/10.1002/2016EA000204, 2017.

Brix, H., Menemenlis, D., Hill, C., Dutkiewicz, S., Jahn, O., Wang, D., Bowman, K., and Zhang, H.: Using Green's Functions to initialize and adjust a global, eddying ocean biogeochemistry general circulation model, Ocean Model., 95, 1-14, https://doi.org/10.1016/j.ocemod.2015.07.008, 2015.

Byrd, R.H., Nocedal, J., and Schnabel, R.B.: Representations of quasi-Newton matrices and their use in limited memory methods, Math. Program., 63, 129-156, https://doi.org/10.1007/BF01582063, 1994.

Byrne, B., Liu, J., et al.: Improved constraints on northern extratropical CO2 fluxes obtained by combining surface-based and space-based atmospheric CO2 measurements, *JGR-Atmosphere*, (*minor revision*), 2020

Carroll, D., Menemenlis, D., Adkins, J. F., Bowman, K. W., Brix, H., Dutkiewicz, S., et al.: The ECCO-Darwin Data-assimilative Global Ocean Biogeochemistry Model: Estimates of Seasonal to Multi-decadal Surface Ocean $pCO_2$ and Air-sea $CO_2$ Flux. *Journal of Advances in Modeling Earth Systems*, 12, e2019MS001888. https://doi.org/10.1029/2019MS001888.2020

Carbontracker Team; (2019) : Compilation of near real time atmospheric carbon dioxide data; obspack_co2_1_NRT_v5.0_2019-08-13; NOAA Earth System Research Laboratory, Global Monitoring Division. http://doi.org/10.25925/20190813

Chevallier, F., Fisher, M., Peylin, P., Serrar, S., Bousquet, P., Bréon, F.M., Chédin, A., and Ciais, P.: Inferring CO2 sources and sinks from satellite observations: Method and application to TOVS data, J. Geophys. Res.-Atmos., 110, D24309, https://doi.org/10.1029/2005JD006390, 2005.

Chevallier, F., Ciais, P., Conway, T.J., Aalto, T., Anderson, B.E., Bousquet, P., Brunke, E.G., Ciattaglia, L., Esaki, Y., Fröhlich, M., and Gomez, A.: $CO_2$ surface fluxes at grid point scale estimated from a global 21 year reanalysis of atmospheric measurements, J. Geophys. Res., 115, D21307, https://doi.org/10.1029/2010JD013887, 2010.

Chevallier, F., Remaud, M., O'Dell, C. W., Baker, D., Peylin, P., and Cozic, A.: Objective evaluation of surface- and satellite-driven carbon dioxide atmospheric inversions, Atmos. Chem. Phys., 19, 14233–14251, https://doi.org/10.5194/acp-19-14233-2019, 2019.

Ciais, P., Tan, J., Wang, X., Roedenbeck, C., Chevallier, F., Piao, S.L., Moriarty, R., Broquet, G., Le Quéré, C., Canadell, J.G., and Peng, S.: Five decades of northern land carbon uptake revealed by the interhemispheric CO 2 gradient, Nature, 568, 221-225, https://doi.org/10.1038/s41586-019-1078-6, 2019.

Conway, T. J., Tans, P. P., Waterman, L. S., Thoning, K. W., Kitzis, D. R., Masarie, K. A., and Zhang, N. (1994), Evidence for interannual variability of the carbon cycle from the National Oceanic and Atmospheric Administration/Climate Monitoring and Diagnostics Laboratory Global Air Sampling Network, *J. Geophys. Res.*, 99( D11), 22831– 22855, doi:10.1029/94JD01951.

Crisp, D., Fisher, B. M., O'Dell, C., Frankenberg, C., Basilio, R., Bösch, H., Brown, L. R., Castano, R., Connor, B., Deutscher, N. M., Eldering, A., Griffith, D., Gunson, M., Kuze, A., Mandrake, L., McDuffie, J., Messerschmidt, J., Miller, C. E., Morino, I., Natraj, V., Notholt, J., O'Brien, D. M., Oyafuso, F., Polonsky, I., Robinson, J., Salawitch, R., Sherlock, V., Smyth, M., Suto, H., Taylor, T. E., Thompson, D. R., Wennberg, P. O., Wunch, D., and Yung, Y. L.: The ACOS $CO_2$ retrieval algorithm – Part II: Global $X_{CO2}$ data characterization, Atmos. Meas. Tech., 5, 687–707, https://doi.org/10.5194/amt-5-687-2012, 2012.

Crisp, D., Pollock, H. R., Rosenberg, R., Chapsky, L., Lee, R. A. M., Oyafuso, F. A., Frankenberg, C., O'Dell, C. W., Bruegge, C. J., Doran, G. B., Eldering, A., Fisher, B. M., Fu, D., Gunson, M. R., Mandrake, L., Osterman, G. B., Schwandner, F. M., Sun, K., Taylor, T. E., Wennberg, P. O., and Wunch, D.: The on-orbit performance of the Orbiting Carbon Observatory-2 (OCO-2) instrument and its radiometrically calibrated products, Atmos. Meas. Tech., 10, 59–81, https://doi.org/10.5194/amt-10-59-2017, 2017.

Crowell, S., Baker, D., Schuh, A., Basu, S., Jacobson, A. R., Chevallier, F., Liu, J., Deng, F., Feng, L., McKain, K., Chatterjee, A., Miller, J. B., Stephens, B. B., Eldering, A., Crisp, D., Schimel, D., Nassar, R., O'Dell, C. W., Oda, T., Sweeney, C., Palmer, P. I., and Jones, D. B. A.: The 2015–2016 carbon cycle as seen from OCO-2 and the global in situ network, Atmos. Chem. Phys., 19, 9797–9831, https://doi.org/10.5194/acp-19-9797-2019, 2019.

Falk, M., Wharton, S., Schroeder, M., Ustin, S., and U, K.T.P.: Flux partitioning in an old-growth forest: seasonal and interannual dynamics. Tree Physiol., 28, 509-520, https://doi.org/10.1093/treephys/28.4.509, 2008.

Fisher, M. and Courtier, P. (1995) Estimating the covariance matrices of analysis and forecast error in variational data assimilation. Technical Memorandum 220. Reading, UK: ECMWF.

Friedlingstein, P., Meinshausen, M., Arora, V.K., Jones, C.D., Anav, A., Liddicoat, S.K., and Knutti, R.: Uncertainties in CMIP5 climate projections due to carbon cycle feedbacks, J. Clim., 27, 511-526, https://doi.org/10.1175/JCLI-D-12-00579.1, 2014.

Friedlingstein, P., Jones, M., O'Sullivan, M., Andrew, R., Hauck, J., Peters, G., Peters, W., Pongratz, J., Sitch, S., Le Quéré, C., and DBakker, O.: Global carbon budget 2019, Earth Syst. Sci. Data, 11, 1783-1838, https://doi.org/10.3929/ethz-b-000385668, 2019.

Gatti, L.V., Gloor, M., Miller, J.B., Doughty, C.E., Malhi, Y., Domingues, L.G., Basso, L.S., Martinewski, A., Correia, C.S.C., Borges, V.F., and Freitas, S., 2014, Drought sensitivity of Amazonian carbon balance revealed by atmospheric measurements, Nature, 506, 76-80, https://doi.org/10.1038/nature12957, 2014.

Gaubert, B., Stephens, B. B., Basu, S., Chevallier, F., Deng, F., Kort, E. A., Patra, P. K., Peters, W., Rödenbeck, C., Saeki, T., Schimel, D., Van der Laan-Luijkx, I., Wofsy, S., and Yin, Y.: Global atmospheric $CO_2$ inverse models converging on neutral tropical land exchange, but disagreeing on fossil fuel and atmospheric growth rate, Biogeosciences, 16, 117–134, https://doi.org/10.5194/bg-16-117-2019, 2019.

Gurney, K.R., Law, R.M., Denning, A.S., Rayner, P.J., Pak, B.C., Baker, D., Bousquet, P., Bruhwiler, L., Chen, Y.H., Ciais, P., and Fung, I.Y.: Transcom 3 inversion intercomparison: Model mean results for the estimation of seasonal carbon sources and sinks, Global Biogeochem. Cycles, 18, GB1010, https://doi.org/10.1029/2003GB002111, 2004.

Henze, D. K., Hakami, A., and Seinfeld, J. H.: Development of the adjoint of GEOS-Chem, Atmos. Chem. Phys., 7, 2413–2433, https://doi.org/10.5194/acp-7-2413-2007, 2007.

Jiang, Z., Worden, J. R., Worden, H., Deeter, M., Jones, D. B. A., Arellano, A. F., and Henze, D. K.: A 15-year record of CO emissions constrained by MOPITT CO observations, Atmos. Chem. Phys., 17, 4565–4583, https://doi.org/10.5194/acp-17-4565-2017, 2017.

Joiner, J., Guanter, L., Lindstrot, R., Voigt, M., Vasilkov, A. P., Middleton, E. M., Huemmrich, K. F., Yoshida, Y., and Frankenberg, C.: Global monitoring of terrestrial chlorophyll fluorescence from moderate-spectral-resolution near-infrared satellite measurements: methodology, simulations, and application to GOME-2, Atmos. Meas. Tech., 6, 2803–2823, https://doi.org/10.5194/amt-6-2803-2013, 2013.

Joiner, J., Yoshida, Y., Zhang, Y., Duveiller, G., Jung, M., Lyapustin, A., Wang, Y., & Tucker, C.: Estimation of terrestrial global gross primary production (GPP) with satellite data-driven models and eddy covariance flux data. *Remote Sensing*, **10**(9), 1346. https://doi.org/10.3390/rs10091346. 2018.

Jones, D. B. A., Bowman, K. W., Logan, J. A., Heald, C. L., Liu, J., Luo, M., Worden, J., and Drummond, J.: The zonal structure of tropical O3 and CO as observed by the Tropospheric Emission Spectrometer in November 2004 – Part 1: Inverse modeling of CO emissions, Atmos. Chem. Phys., 9, 3547–3562, https://*doi*.org/*10.5194*/*acp-9-3547-2009* , 2009.

Jung, Martin, et al.: "Compensatory water effects link yearly global land CO 2 sink changes to temperature." *Nature* 541.7638 (2017): 516-520.

Kiel, M., O'Dell, C. W., Fisher, B., Eldering, A., Nassar, R., MacDonald, C. G., and Wennberg, P. O.: How bias correction goes wrong: measurement of $X_{CO2}$ affected by erroneous surface pressure estimates, Atmos. Meas. Tech., 12, 2241–2259, https://doi.org/10.5194/amt-12-2241-2019, 2019.

Konings, A. G., Bloom, A. A., Liu, J., Parazoo, N. C., Schimel, D. S., and Bowman, K. W.: Global satellite-driven estimates of heterotrophic respiration, Biogeosciences, 16, 2269–2284, https://doi.org/10.5194/bg-16-2269-2019, 2019.

Kulawik, S. S., Crowell, S., Baker, D., Liu, J., McKain, K., Sweeney, C., Biraud, S. C., Wofsy, S., O'Dell, C. W., Wennberg, P. O., Wunch, D., Roehl, C. M., Deutscher, N. M., Kiel, M., Griffith, D. W. T., Velazco, V. A., Notholt, J., Warneke, T., Petri, C., De Mazière, M., Sha, M. K., Sussmann, R., Rettinger, M., Pollard, D. F., Morino, I., Uchino, O., Hase, F., Feist, D. G., Roche, S., Strong, K., Kivi, R., Iraci, L., Shiomi, K., Dubey, M. K., Sepulveda, E., Rodriguez, O. E. G., Té, Y., Jeseck, P., Heikkinen, P., Dlugokencky, E. J., Gunson, M. R., Eldering, A., Crisp, D., Fisher, B., and Osterman, G. B.: Characterization of OCO-2 and ACOS-GOSAT biases and errors for $CO_2$ flux estimates, Atmos. Meas. Tech. Discuss., https://doi.org/10.5194/amt-2019-257, in review, 2019.

Kuze, A., Suto, H., Shiomi, K., Kawakami, S., Tanaka, M., Ueda, Y., Deguchi, A., Yoshida, J., Yamamoto, Y., Kataoka, F., Taylor, T. E., and Buijs, H. L.: Update on GOSAT TANSO-FTS performance, operations, and data products after more than 6 years in space, Atmos. Meas. Tech., 9, 2445–2461, https://doi.org/10.5194/amt-9-2445-2016, 2016.

Le Quéré, C., Andrew, R. M., Friedlingstein, P., Sitch, S., Pongratz, J., Manning, A. C., Korsbakken, J. I., Peters, G. P., Canadell, J. G., Jackson, R. B., Boden, T. A., Tans, P. P., Andrews, O. D., Arora, V. K., Bakker, D. C. E., Barbero, L., Becker, M., Betts, R. A., Bopp, L., Chevallier, F., Chini, L. P., Ciais, P., Cosca, C. E., Cross, J., Currie, K., Gasser, T., Harris, I., Hauck, J., Haverd, V., Houghton, R. A., Hunt, C. W., Hurtt, G., Ilyina, T., Jain, A. K., Kato, E., Kautz, M., Keeling, R. F., Klein Goldewijk, K., Körtzinger, A., Landschützer, P., Lefèvre, N., Lenton, A., Lienert, S., Lima, I., Lombardozzi, D., Metzl, N., Millero, F., Monteiro, P. M. S., Munro, D. R., Nabel, J. E. M. S., Nakaoka, S., Nojiri, Y., Padin, X. A., Peregon, A., Pfeil, B., Pierrot, D., Poulter, B., Rehder, G., Reimer, J., Rödenbeck, C., Schwinger, J., Séférian, R., Skjelvan, I., Stocker, B. D., Tian, H., Tilbrook, B., Tubiello, F. N., van der Laan-Luijkx, I. T., van der Werf, G. R., van Heuven, S., Viovy, N., Vuichard, N., Walker, A. P., Watson, A. J., Wiltshire, A. J., Zaehle, S., and Zhu, D.: Global Carbon Budget 2017, Earth Syst. Sci. Data, 10, 405–448, https://doi.org/10.5194/essd-10-405-2018, 2018.

Liu, J., Baskarran, L., Bowman, K., Schimel, D., Bloom, A. A., Parazoo, N., Oda, T., Carrol, D., Menemenlis, D., Joiner, J., Commane, R., Daube, B., Gatti, L. V., McKain, K., Miller, J., Stephens, B. B., Sweeney, C., & Wofsy, S. (2020). *CMS-Flux NBE 2020* [Data set]. NASA. https://doi.org/10.25966/4V02-C391

Liu, J. and Bowman, K.: A method for independent validation of surface fluxes from atmospheric inversion: Application to CO2, Geophys. Res. Lett., 43, 3502-3508, https://doi.org/10.1002/2016GL067828, 2016.

Liu, J., Bowman, K. W., and Henze, D. K.: Source-receptor relationships of column-average $CO_2$and implications for the impact of observations on flux inversions. *J. Geophys. Res. Atmos.*, 120, 5214– 5236. doi: 10.1002/2014JD022914, 2015

Liu, J., Bowman, K.W., Lee, M., Henze, D.K., Bousserez, N., Brix, H., James Collatz, G., Menemenlis, D., Ott, L., Pawson, S., and Jones, D.: Carbon monitoring system flux estimation and attribution: impact of ACOS-GOSAT XCO2 sampling on the inference of terrestrial biospheric sources and sinks. Tellus B Chem. Phys. Meteorol. B., 66, 22486, http://dx.doi.org/10.3402/tellusb.v66.22486, 2014.

Liu, J., Bowman, K.W., Schimel, D.S., Parazoo, N.C., Jiang, Z., Lee, M., Bloom, A.A., Wunch, D., Frankenberg, C., Sun, Y., and O'Dell, C.W.: Contrasting carbon cycle responses of the tropical continents to the 2015–2016 El Niño. Science, 358, eaam5690, https://doi.org/10.1126/science.aam5690, 2017.

Liu, J., Bowman, K., Parazoo, N.C., Bloom, A.A., Wunch, D., Jiang, Z., Gurney, K.R., and Schimel, D.: Detecting drought impact on terrestrial biosphere carbon fluxes over contiguous US with satellite observations. Environ. Res. Lett., 13, 095003, https://doi.org/10.1088/1748-9326/aad5ef, 2018.

Liu, Z.-Q. and Rabier, F. (2003), The potential of high-density observations for numerical weather prediction: A study with simulated observations. Q.J.R. Meteorol. Soc., 129: 3013-3035. doi:10.1256/qj.02.170

Lorenc, A. C., 1981: A Global Three-Dimensional Multivariate Statistical Interpolation Scheme. *Mon. Wea. Rev.*, **109**, 701–721

Lovenduski, N.S. and Bonan, G.B.: Reducing uncertainty in projections of terrestrial carbon uptake, Environ. Res. Lett., 12, 044020, https://doi.org/10.1088/1748-9326/aa66b8, 2017.

Meirink, J.F., Bergamaschi, P. and Krol, M.C. (2008) Four-dimensional variational data assimilation for inverse modelling of atmospheric methane emissions: method and comparison with synthesis inversion, Atmos. *Chem. Phys.*, **8**, 6341– 6353, https://doi.org/10.5194/acp-8-6341-2008.

Nassar, R., Jones, D.B., Suntharalingam, P., Chen, J.M., Andres, R.J., Wecht, K.J., Yantosca, R.M., Kulawik, S.S., Bowman, K.W., Worden, J.R., and Machida, T.: Modeling global atmospheric CO2 with improved emission inventories and CO2 production from the oxidation of other carbon species. Geosci. Model Dev., 3, 689-716, https://doi.org/10.5194/gmd-3-689-2010, 2010.

Niwa, Y, Fujii, Y. A conjugate BFGS method for accurate estimation of a posterior error covariance matrix in a linear inverse problem. *Q J R Meteorol Soc*. 2020; 1– 26. https://doi.org/10.1002/qj.3838

Oda, T., Maksyutov, S., and Andres, R. J.: The Open-source Data Inventory for Anthropogenic $CO_2$, version 2016 (ODIAC2016): a global monthly fossil fuel $CO_2$ gridded emissions data product for tracer transport simulations and surface flux inversions, Earth Syst. Sci. Data, 10, 87–107, https://doi.org/10.5194/essd-10-87-2018, 2018.

O'Dell, C. W., Connor, B., Bösch, H., O'Brien, D., Frankenberg, C., Castano, R., Christi, M., Eldering, D., Fisher, B., Gunson, M., McDuffie, J., Miller, C. E., Natraj, V., Oyafuso, F., Polonsky, I., Smyth, M., Taylor, T., Toon, G. C., Wennberg, P. O., and Wunch, D.: The ACOS $CO_2$ retrieval algorithm – Part 1: Description and validation against synthetic observations, Atmos. Meas. Tech., 5, 99–121, https://doi.org/10.5194/amt-5-99-2012, 2012.

O'Dell, C., Eldering, A., Wennberg, P.O., Crisp, D., Gunson, M., Fisher, B., Frankenberg, C., Kiel, M., Lindqvist, H., Mandrake, L., and Merrelli, A.: Improved retrievals of carbon dioxide from Orbiting Carbon Observatory-2 with the version 8 ACOS algorithm, Atmos. Meas. Tech., 11, 6539–6576, https://doi.org/10.5194/amt-11-6539-2018, 2018.

Olsen, S.C. and Randerson, J.T.: Differences between surface and column atmospheric CO2 and implications for carbon cycle research, J. Geophys. Res: Atmos., 109, D02301, https://doi.org/10.1029/2003JD003968, 2004.

Parazoo, N.C., Bowman, K., Fisher, J.B., Frankenberg, C., Jones, D.B.A., Cescatti, A., Pérez-Priego, Ó., Wohlfahrt, G. and Montagnani, L.: Terrestrial gross primary production inferred from satellite fluorescence and vegetation models. Glob Change Biol, 20: 3103-3121. doi:10.1111/gcb.12652. 2014.

Peylin, P., Law, R. M., Gurney, K. R., Chevallier, F., Jacobson, A. R., Maki, T., Niwa, Y., Patra, P. K., Peters, W., Rayner, P. J., Rödenbeck, C., van der Laan-Luijkx, I. T., and Zhang, X.: Global atmospheric carbon budget: results from an ensemble of atmospheric $CO_2$ inversions, Biogeosciences, 10, 6699–6720, https://doi.org/10.5194/bg-10-6699-2013, 2013.

Peters, W., et al. (2007), An atmospheric perspective on North American carbon dioxide exchange: CarbonTracker, *Proc. Natl. Acad. Sci. U. S. A.*, **104**(48), 18,925– 18,930, doi:10.1073/pnas.0708986104.

Peters, W., Krol, M. C., Van Der Werf, G.R., et al, 2010, Seven years of recent European net terrestrial carbon dioxide exchange constrained by atmospheric observations. Global Change Biology, 16: 1317-1337. doi:10.1111/j.1365-2486.2009.02078.x

Poulter, B., Frank, D., Ciais, P., Myneni, R.B., Andela, N., Bi, J., Broquet, G., Canadell, J.G., Chevallier, F., Liu, Y.Y., and Running, S.W.: Contribution of semi-arid ecosystems to interannual variability of the global carbon cycle, Nature, 509, 600-603, https://doi.org/10.1038/nature13376, 2014.

Quetin, G., Bloom, A. A., Bowman, K. W., & Konings, A.: Carbon flux variability from a relatively simple ecosystem model with assimilated data is consistent with terrestrial biosphere model estimates. *Journal of Advances in Modeling Earth Systems*, 12, e2019MS001889. https://doi.org/10.1029/2019MS001889, 2020

Randerson, J.T., Van Der Werf, G.R., Giglio, L., Collatz, G.J., and Kasibhatla, P.S.: Global Fire Emissions Database, Version 4.1 (GFEDv4), ORNL DAAC, Oak Ridge, Tennessee, USA, https://doi.org/10.3334/ORNLDAAC/1293, 2018.

Rienecker, M.M., Suarez, M.J., Gelaro, R., Todling, R., Bacmeister, J., Liu, E., Bosilovich, M.G., Schubert, S.D., Takacs, L., Kim, G.K., and Bloom, S.: MERRA: NASA's modern-era retrospective analysis for research and applications, J. Clim., 24, 3624-3648, https://doi.org/10.1175/JCLI-D-11-00015.1, 2011.

Rödenbeck, C., Houweling, S., Gloor, M., and Heimann, M.: $CO_2$ flux history 1982–2001 inferred from atmospheric data using a global inversion of atmospheric transport, Atmos. Chem. Phys., 3, 1919–1964, https://doi.org/10.5194/acp-3-1919-2003, 2003.

Running, S.W., Baldocchi, D.D., Turner, D.P., Gower, S.T., Bakwin, P.S., and Hibbard, K.A.: A global terrestrial monitoring network integrating tower fluxes, flask sampling, ecosystem modeling and EOS satellite data, Remote Sens. Environ., 70, 108-127, https://doi.org/10.1016/S0034-4257(99)00061-9, 1999.

Schuh, A.E., Jacobson, A.R., Basu, S., Weir, B., Baker, D., Bowman, K., Chevallier, F., Crowell, S., Davis, K.J., Deng, F., and Denning, S.: Quantifying the impact of atmospheric transport uncertainty on CO2 surface flux estimates, Global Biogeochem. Cy., 33, 484-500, https://doi.org/10.1029/2018GB006086, 2019.

Sellers, P.J., Schimel, D.S., Moore, B., Liu, J., and Eldering, A.: Observing carbon cycle–climate feedbacks from space, PNAS, 115, 7860-7868, https://doi.org/10.1073/pnas.1716613115, 2018.

Stephens, B.B., Gurney, K. R., Tans, P. P., *et al*.:. Weak northern and strong tropical land carbon uptake from vertical profiles of atmospheric $CO_2$. *Science* **316**: 1732– 35, doi:10.1126/science.1137004. 2007

Stephens, B., et al. 2017. ORCAS Airborne Oxygen Instrument. Version 1.0. UCAR/NCAR - Earth Observing Laboratory. https://doi.org/10.5065/D6N29VC6.

Sweeney, C., Karion, A., Wolter, S., et al.: Seasonal climatology of $CO_2$ across North America from aircraft measurements in the NOAA/ESRL Global Greenhouse Gas Reference Network. *J. Geophys. Res. Atmos.*, 120, 5155– 5190. doi: 10.1002/2014JD022591. 2015

Suntharalingam, P., Jacob, D.J., Palmer, P.I., Logan, J.A., Yantosca, R.M., Xiao, Y., Evans, M.J., Streets, D.G., Vay, S.L., and Sachse, G.W.: Improved quantification of Chinese carbon fluxes using CO2/CO correlations in Asian outflow, J. Geophys. Res.: Atmos., 109, D18S18, https://doi.org/10.1029/2003JD004362, 2004.

Tramontana, G., Jung, M., Schwalm, C. R., Ichii, K., Camps-Valls, G., Ráduly, B., Reichstein, M., Arain, M. A., Cescatti, A., Kiely, G., Merbold, L., Serrano-Ortiz, P., Sickert, S., Wolf, S., and Papale, D.: Predicting carbon dioxide and energy fluxes across global FLUXNET sites with regression algorithms, Biogeosciences, 13, 4291–4313, https://doi.org/10.5194/bg-13-4291-2016, 2016.

van der Laan-Luijkx et al, 2017, "The CarbonTracker Data Assimilation Shell (CTDAS) v1.0: implementation and global carbon balance 2001-2015", Geosci. Model Dev., 10, 2785-2800,

van der Werf, G. R., Randerson, J. T., Giglio, L., Gobron, N., and Dolman, A. J.: Climate controls on the variability of fires in the tropics and subtropics, *Global Biogeochem. Cycles*, 22, GB3028, doi:10.1029/2007GB003122. 2008

Wofsy, S. C.: HIAPER Pole-to-Pole Observations (HIPPO): Fine-grained, global-scale measurements of climatically important atmospheric gases and aerosols, Philos. Trans. R. Soc. A-Math. Phys. Eng. Sci., 369, 2073– 2086, https://doi.org/10.1098/rsta.2010.0313, 2011.

Wofsy, S.C., Afshar, S., Allen, H.M., Apel, E., Asher, E.C., Barletta, B., Bent, J., Bian, H., Biggs, B.C., Blake, D.R., and Blake, N.: ATom: Merged Atmospheric Chemistry, Trace Gases, and Aerosols, ORNL DAAC, Oak Ridge, Tennessee, USA, https://doi.org/10.3334/ORNLDAAC/1581, 2018.

Wunch, D., Toon, G.C., Blavier, J.F.L., Washenfelder, R.A., Notholt, J., Connor, B.J., Griffith, D.W., Sherlock, V., and Wennberg, P.O.: The total carbon column observing network, Philos. Trans. R. Soc. A, 369, 2087-2112, https://doi.org/10.1098/rsta.2010.0240, 2011.

Yin, Y., Bowman, K., Bloom, A.A., and Worden, J.: Detection of fossil fuel emission trends in the presence of natural carbon cycle variability, Environ. Res. Lett., 14, 084050, https://doi.org/10.1088/1748-9326/ab2dd7, 2019.

Zhu, C., Byrd, R.H., Lu, P., and Nocedal, J.: Algorithm 778: L-BFGS-B: Fortran subroutines for large-scale bound-constrained optimization, ACM Trans. Math. Softw., 23, 550-560, https://doi.org/10.1145/279232.279236, 1997.

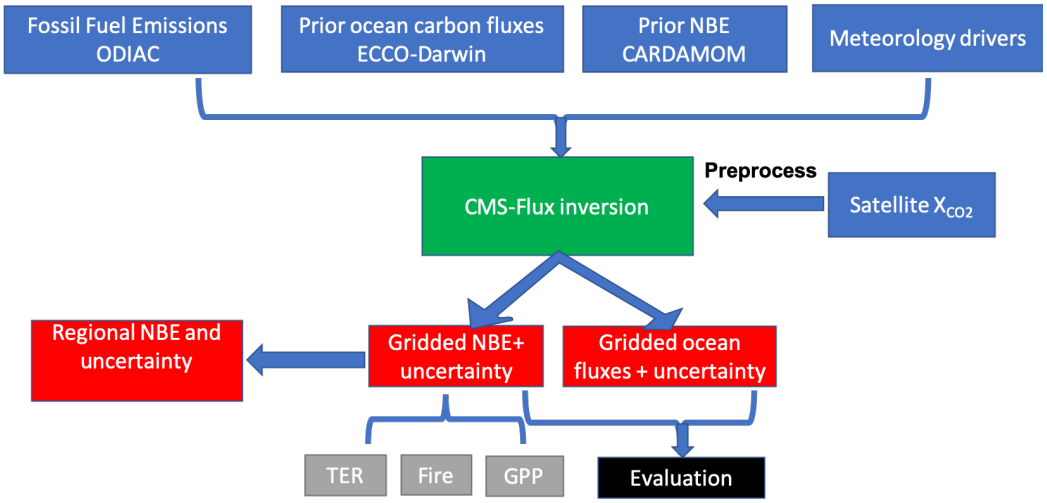


**Figure: 1 Data flow diagram with the main processing steps to generate regional net biosphere change (NBE). TER: total ecosystem respiration; GPP: gross primary production. The green box is the inversion system. The blue boxes are the inputs for the inversion system. The red boxes are the data outputs from the system. The black box is the evaluation step, and the grey boxes are the future additions to the product.**

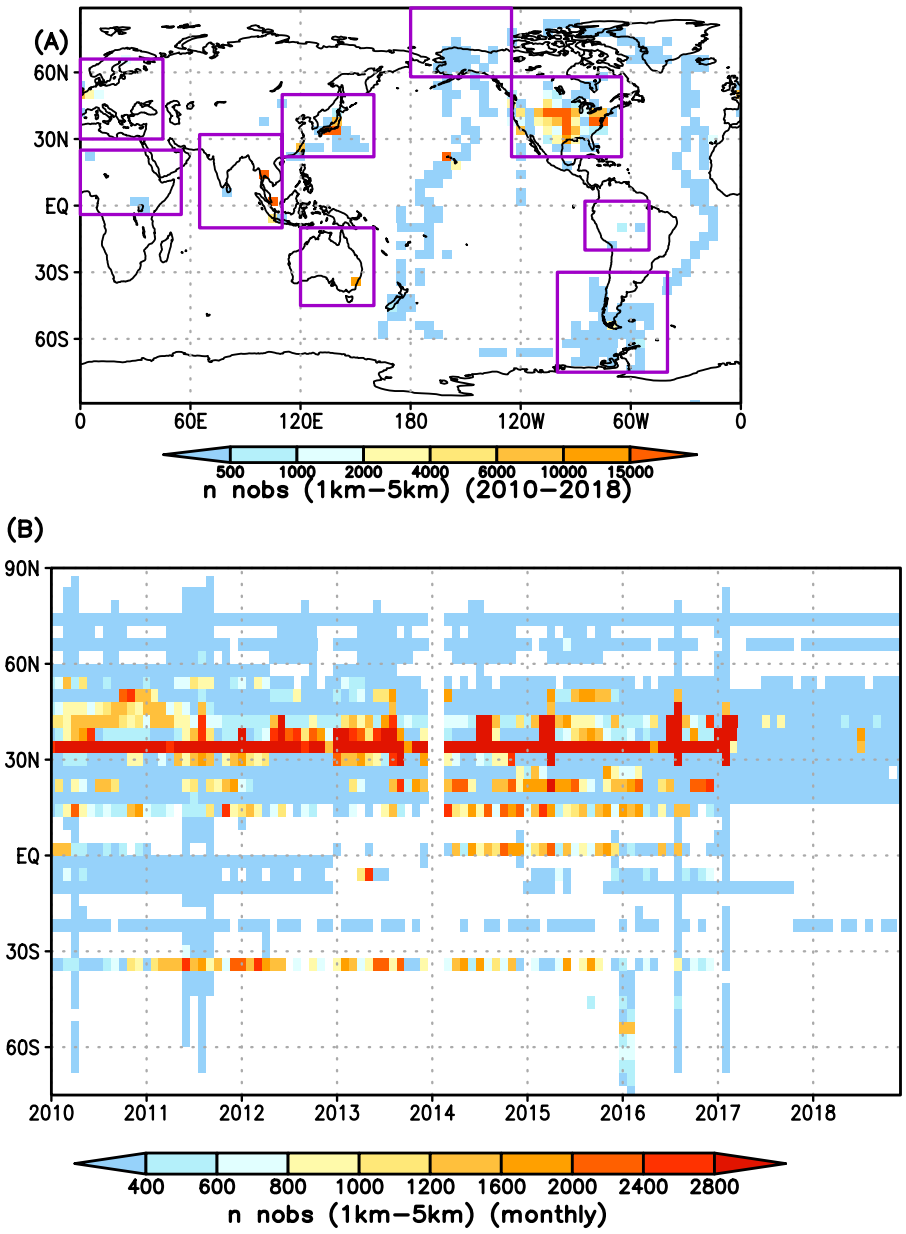


1093

1094 **Figure: 2 The spatial and temporal distributions of aircraft observations used in evaluation**
1095 **of posterior NBE. (A) The total number of aircraft observations between 1–5 km between**
1096 **2010–2018 at each 4° x 5°grid point. The rectangle boxes show the range of the nine sub**
1097 **regions. (B) The total number of monthly aircraft observations at each longitude as a**
1098 **function of time**.
1099

1100

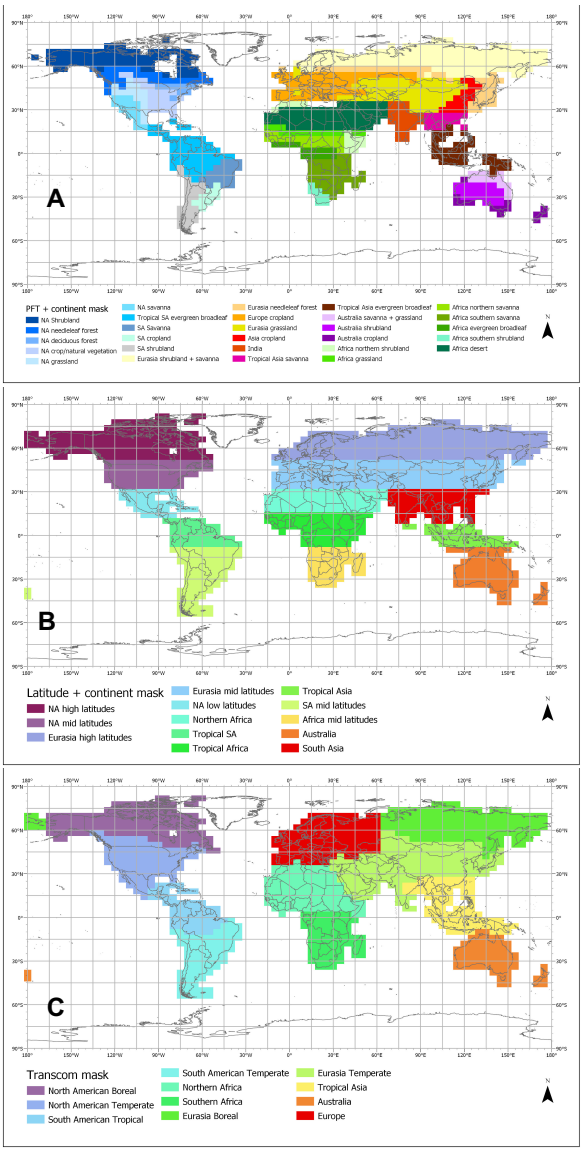


**Figure: 3 Three types of regional masks used in calculating regional fluxes. A: the mask is based on a combination of condensed seven MODIS IGBP plant functional types, TRANCOM-3 regions (Gurney et al., 2004), and continents. B: the mask is based on latitude and continents. C: the TransCom region mask.**

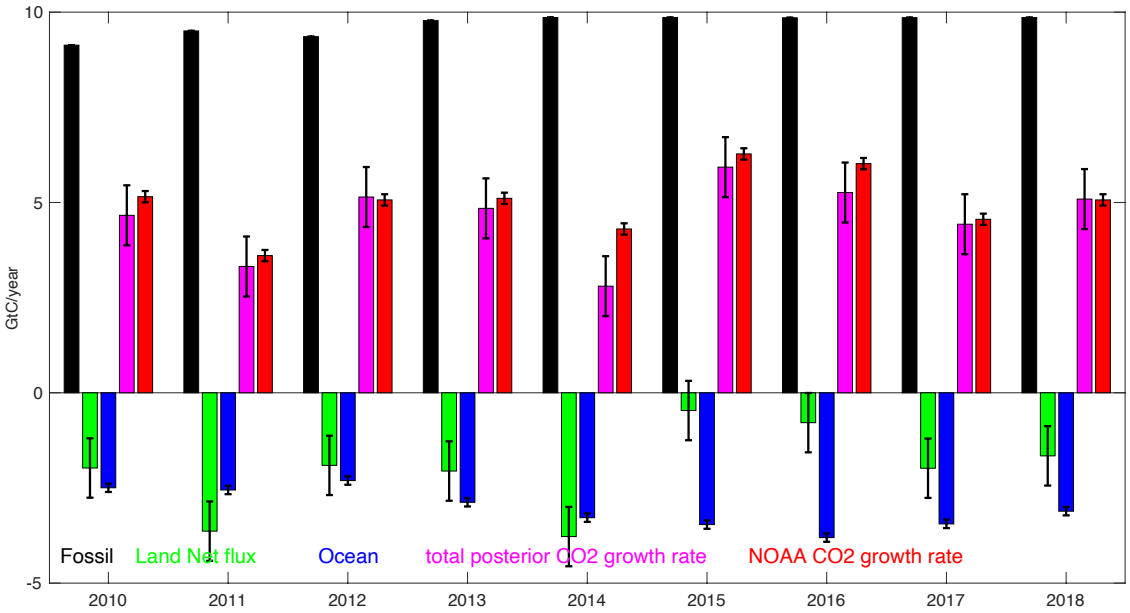


**Figure: 4 Global flux estimation and uncertainties from 2010 –2018 (black: fossil fuel; green: posterior land fluxes; blue: ocean fluxes; magenta: estimated $CO_2$ growth rate; red: the NOAA $CO_2$ growth rate).**

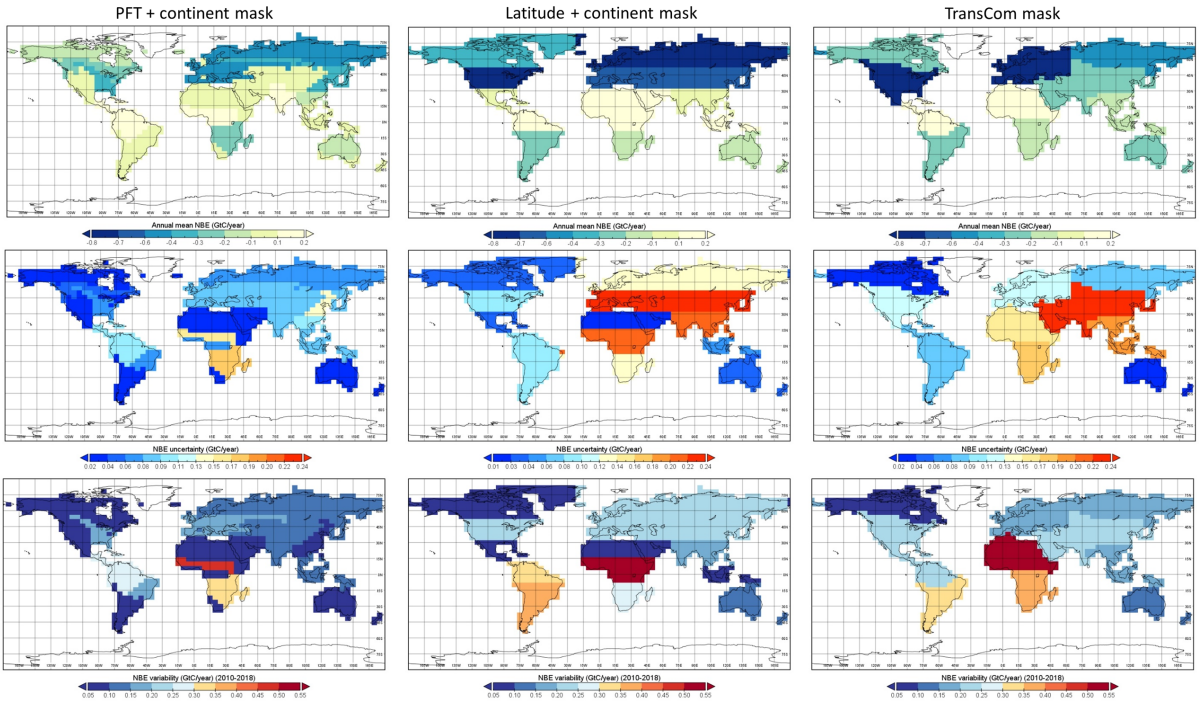


**Figure: 5 Mean annual regional NBE (A, B, and C), uncertainty (D, E, and F), and variability between 2010–2018 (G, H, and I) with the three types of regional masks (Figure 3). The first column uses a region mask based on PFT and continents (RM1). The second column uses a region mask based latitude and continents (RM2), and the third column uses TransCom mask.**

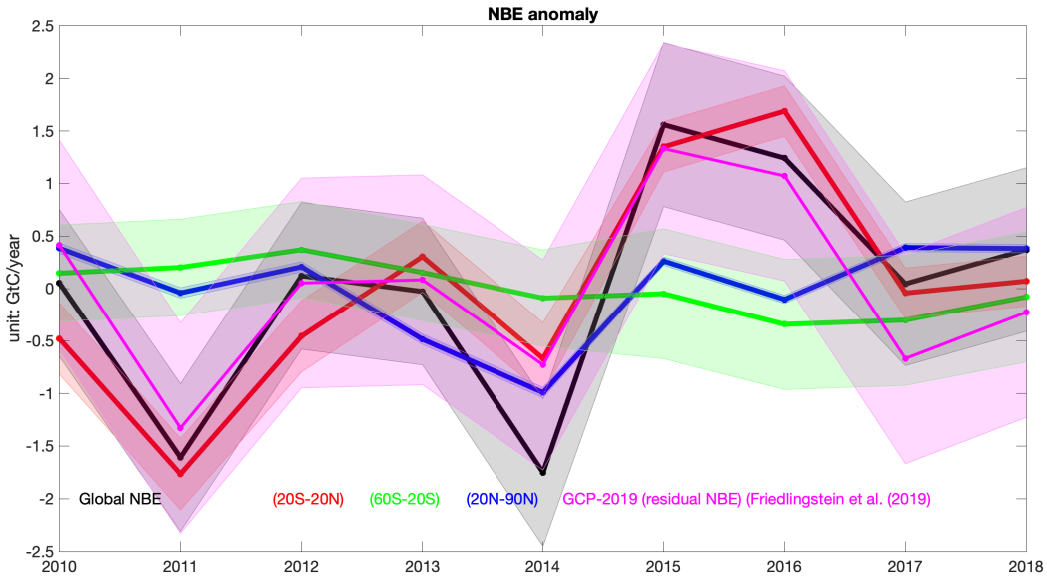


**Figure: 6 The NBE interannual variability over the globe (black), the tropics (20°S–20°N), SH mid-latitudes (60°S–20°S), and NH mid-latitudes (20°N–9°0N). For reference, the residual net land carbon sink from GCP (Friedlingstein et al., 2019) and its uncertainty is also shown (magenta).**

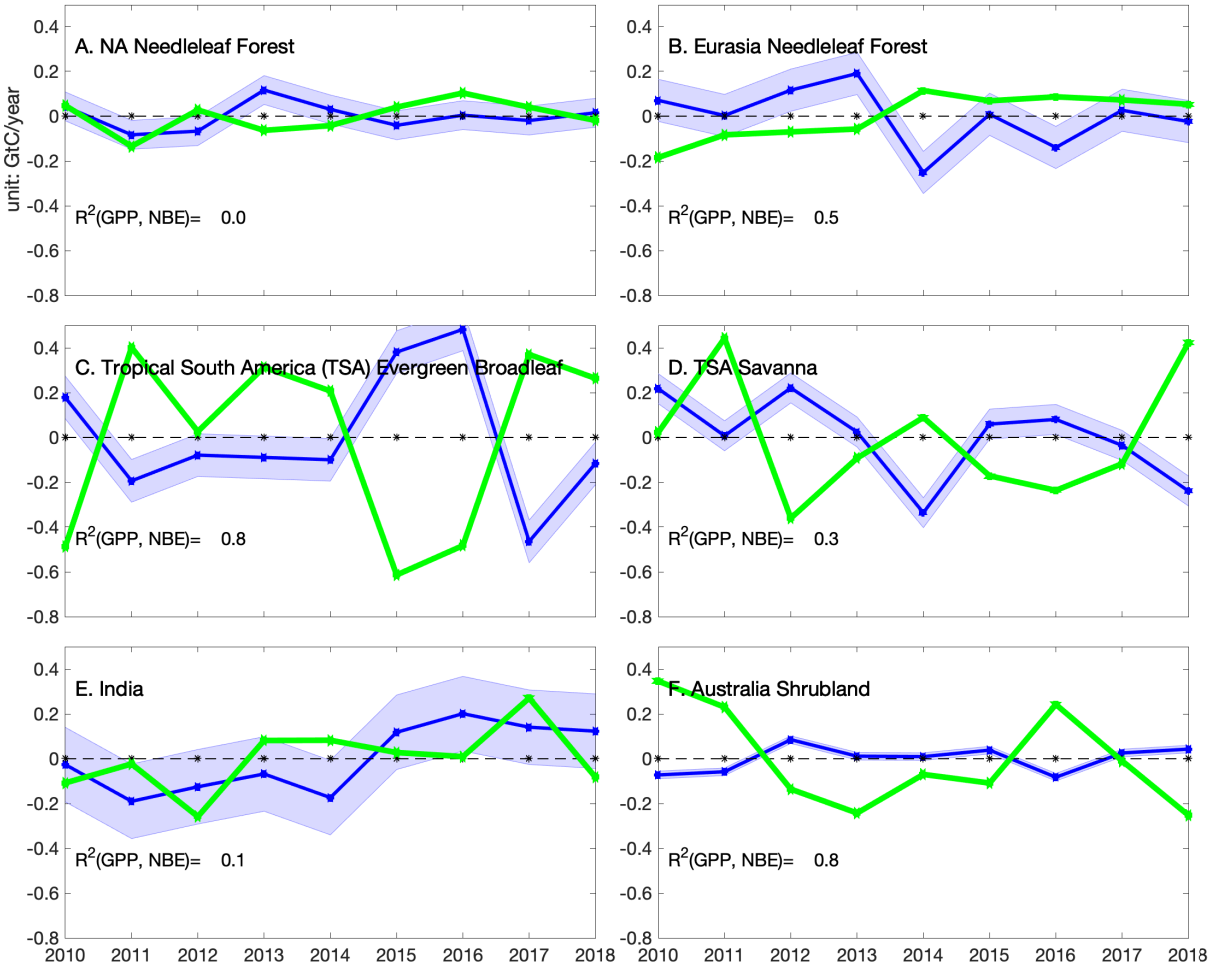


**Figure: 7 The NBE interannual variability over six selected regions. Blue: annual NBE anomaly and its uncertainties. Green: annual GPP anomaly based on FLUXSAT.**

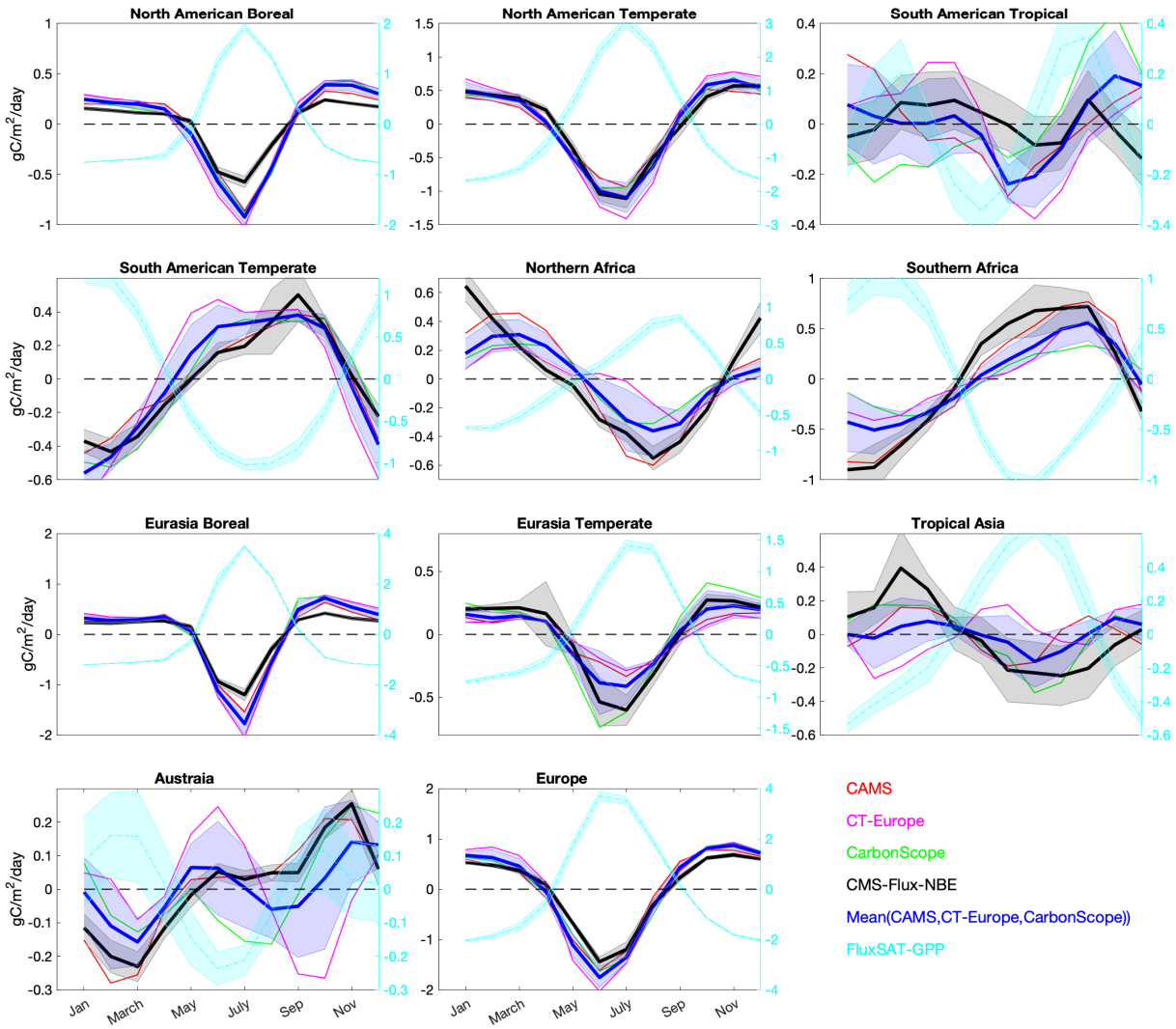


**Figure: 8 The NBE climatological seasonality over TransCom regions. The seasonal cycle is calculated over 2010-2017 since CT-Europe only covers till 2017. Black: CMS-Flux-NBE and its uncertainty; blue shaded: mean NBE seasonality based on surface $CO_2$ inversion results from CAMS, CT-Europe, and Jena CarbonScope; red: CAMS; magenta: CT-Europe; green: Jena CarbonScope. The names of each region are shown on individual subplots.**

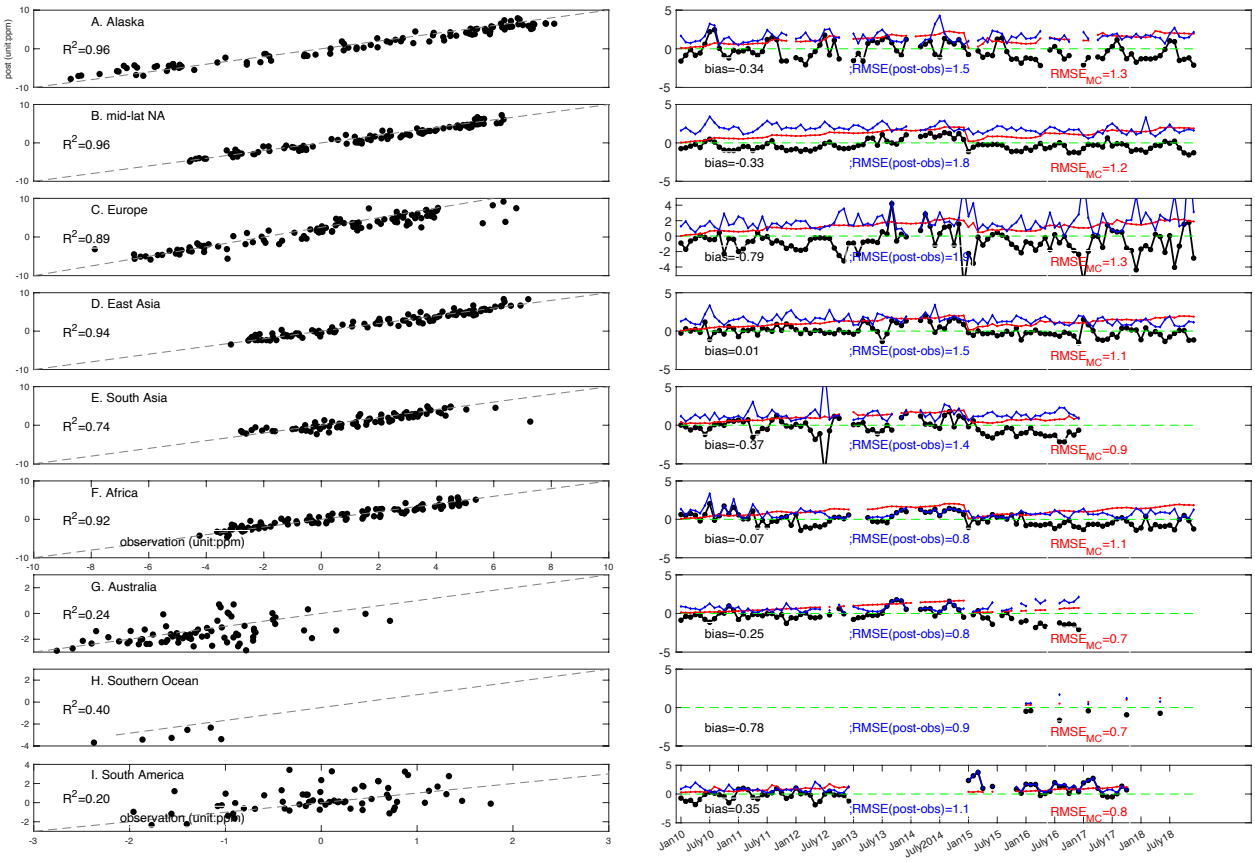


**Figure: 9 Comparison between posterior $CO_2$ mole fraction and aircraft observations. Left panel: detrended posterior $CO_2$ (y-axis) vs. detrended aircraft $CO_2$ (x-axis) over nine regions. The dashed line is 1:1 line; right panel: black: the differences between posterior $CO_2$ and aircraft $CO_2$ as a function of time; blue: RMSE (unit: ppm); red: $RMSE_{MC}$.**

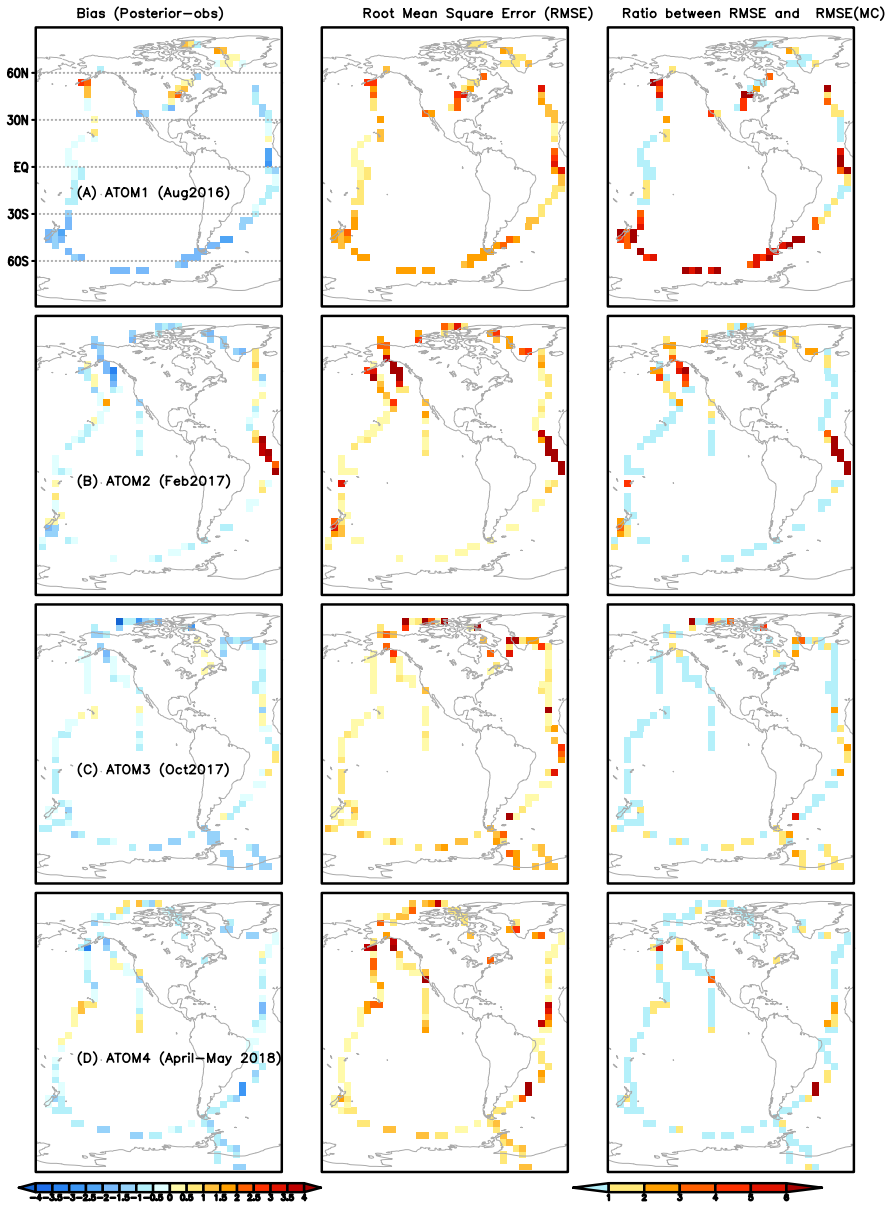


**Figure: 10 Left column: the mean differences between posterior $CO_2$ and aircraft observations from ATOM 1–4 aircraft campaigns between 1–5 km (A–D). Middle column: the Root Mean Square Errors (RMSE) between aircraft observations and posterior $CO_2$ between 1–5 km. The color bar is the same as the left column. Right column: the ratio between RMSE and $RMES_{MC}$ based on ensemble $CO_2$ from the Monte Carlo uncertainty estimation method.**

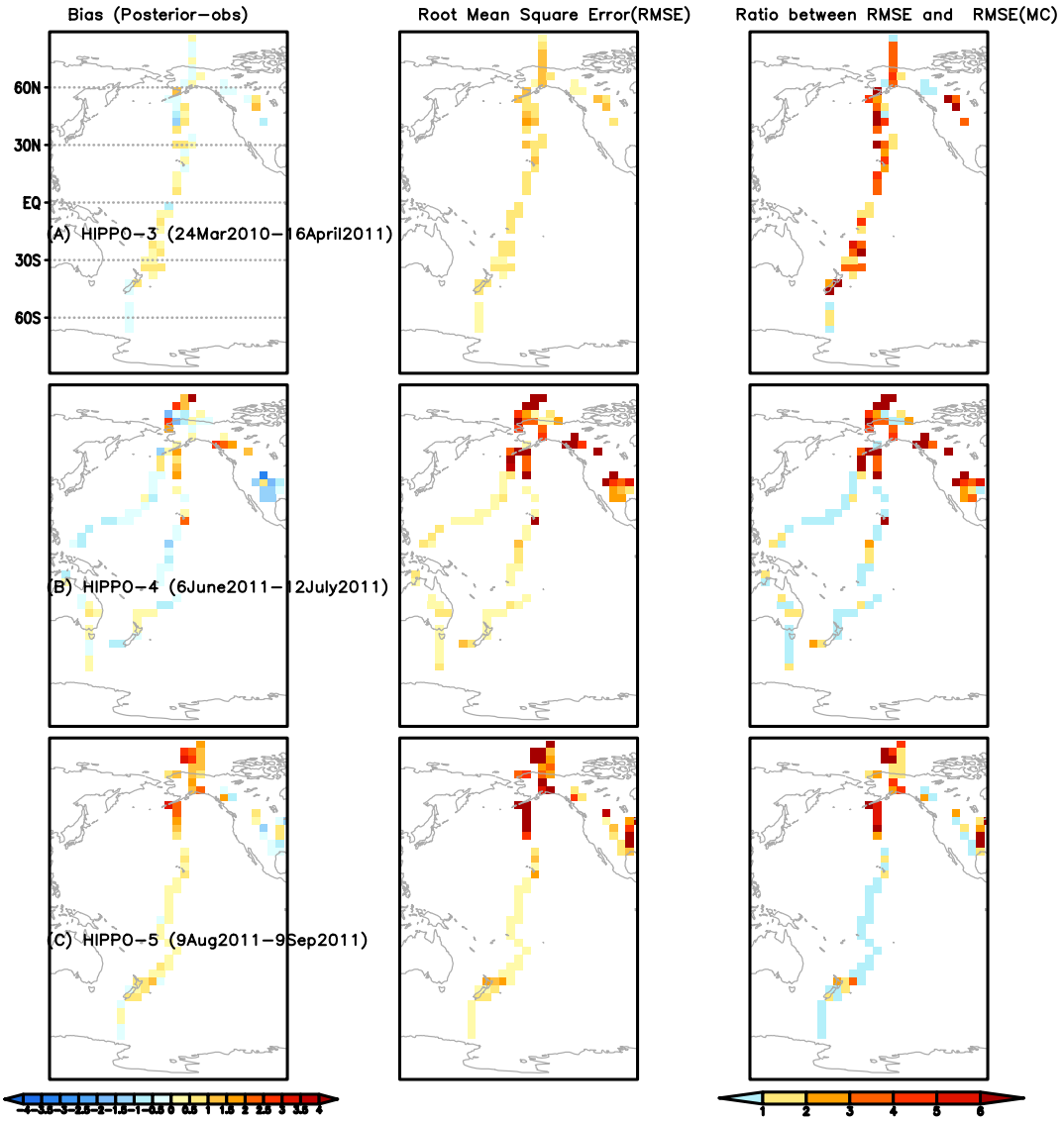


1170

1171 **Figure: 11 Left column: the mean differences between posterior $CO_2$ and aircraft**
1172 **observations from HIPPO 3-5 aircraft campaigns between 1–5 km (A–C) (unit: ppm). (unit:**
1173 **ppm). The time frame of each campaign is in the figure. Middle column: the Root Mean**
1174 **Square Errors (RMSE) between aircraft observations and posterior $CO_2$ between 1–5 km**
1175 **(unit: ppm). The color bar is the same as the left column. Right column: the ratio between**
1176 **RMSE and $RMSE_{MC}$ based on ensemble $CO_2$ from the Monte Carlo method.**
1177
1178

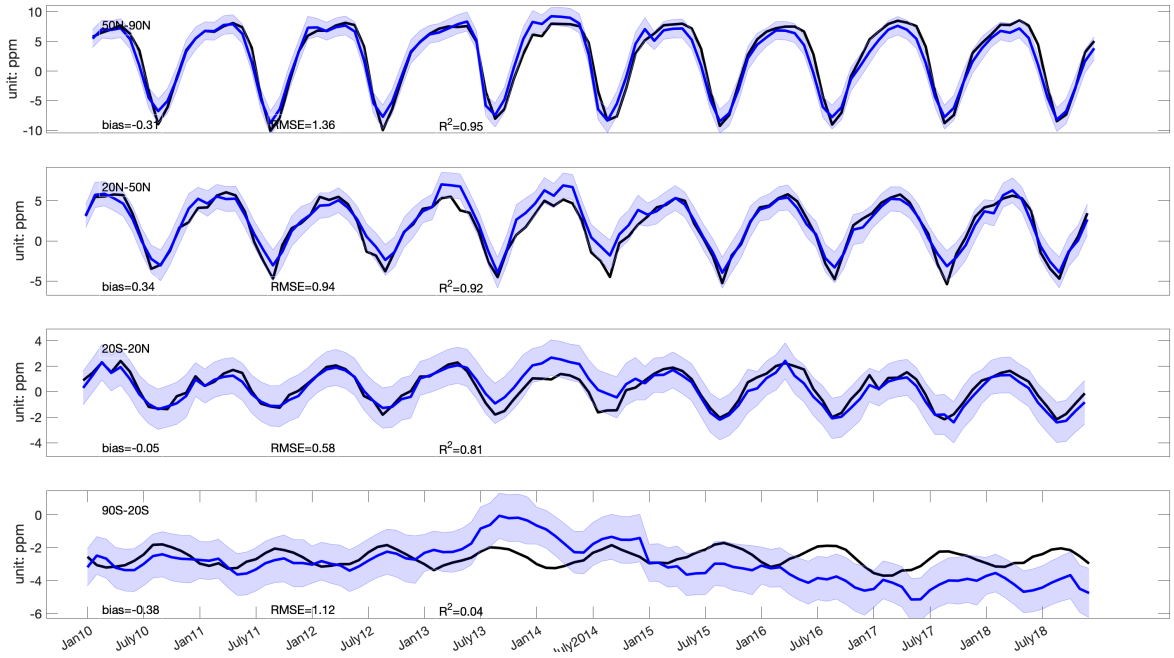


**Figure: 12 Comparison between posterior $CO_2$ and the NOAA marine boundary layer (MBL) reference sites. Black: observations averaged over each latitude bands; blue and shaded area: posterior $CO_2$ and its uncertainty. The global mean $CO_2$ (https://www.esrl.noaa.gov/gmd/ccgg/trends/global.html ) was subtracted from both the NOAA MBL reference and posterior $CO_2$ before the comparison.**

**Table: 1 Configurations of the CMS-Flux atmospheric inversion system**

| | Model setup | Configuration | Reference |
|---|---|---|---|
| **Inversion general setup** | Spatial scale | Global | -- |
| | Spatial resolution | 4° latitude x 5° longitude | |
| | Time resolution | monthly | |
| | Minimizer of cost function | L-BFGS | Byrd et al., 1994; Zhu et al., 1997 |
| | Control vector | Monthly net terrestrial biosphere fluxes and ocean fluxes | |
| **Transport model** | Model name | GEOS-Chem and its adjoint | Suntharalingam et al., 2004<br>Nassar et al., 2010<br>Henze et al., 2007 |
| | Meteorological forcing | GEOS-5 (2010–2014) and GEOS-FP (2015–2019) | Rienecker et al., 2008 |

**Table: 2 Description of the prior fluxes and assumed uncertainties in the inversion system**

| **Prior fluxes** | **Terrestrial biosphere fluxes** | **Ocean fluxes** | **Fossil fuel emissions** |
|---|---|---|---|
| **Model name** | CARDAMOM-v1 | ECCO-Darwin | ODIAC 2018 |
| **Spatial resolution** | 4° x 5° | 0.5° | 1° x 1° |
| **Frequency** | 3-hourly | 3-hourly | hourly |
| **Uncertainty** | Estimated from CARDAMOM | 100% same as Liu et al. (2017) | No uncertainty |
| **References** | Bloom et al., 2006; 2020 | Brix et al, 2015; Carroll et al., 2020 | Oda et al., 2016; 2018 |

1199

1200

1201 **Table: 3 Description of observation and evaluation dataset. Data sources are listed in Table 7.**

| | Dataset name and version | References |
|---|---|---|
| Satellite $X_{CO2}$ | ACOS-GOSAT v7.3 | O'Dell et al., (2012) |
| | OCO-2 v9 | O'Dell et al., (2018) |
| Aircraft $CO_2$ observations | ObsPack OCO-2 MIP | CarbonTracker team (2019) |
| | HIPPO 3-5 | Wofsy et al. (2011) |
| | ATom 1-4 | Wofsy et al. (2018) |
| | INPE | Gatti et al., (2014) |
| | ORCAS | Stephens et al. (2017) |
| NOAA marine boundary layer (MBL) reference | NOAA MBL reference | Conway et al., 1994 |
| GPP | FLUXSAT-GPP | Joiner et al., (2018) |
| Top-down NBE estimates constrained by surface $CO_2$ | CarbonTracker-Europe | van der Laan-Luijkx et al. (2017)<br>Peters et al., (2010)<br>Peters et al. (2007) |
| | Jena CarbonScope s10oc_v2020 | Rödenbeck et al., 2003 |
| | CAMS v18r1 | Chevallier et al., 2005 |

1202

**Table: 4 Latitude and longitude ranges for seven sub regions.**

| Region | Alaska | Mid-lat NA | Europe | East Asia | South Asia |
|---|---|---|---|---|---|
| **Longitude range** | 180°W–125° W | 125°W–65°W | 5°W–45°E | 110°E–160°E | 65°E–110°E |
| **Latitude range** | 58°N–89°N | 22°N-58°N | 30°N–66°N | 22°N–50°N | 10°S–32°N |
| **Region** | Africa | South America | Australia | Southern Ocean | |
| **Longitude range** | 5°W–55°E | 95°W–50°W | 120°E–160°E | 110°W–40°E | |
| **Latitude range** | 2°N–18°N | 20°S–2°N | 45°S–10°S | 80°S–30°S | |

1208 **Table: 5 List of the data products.**

| Product | Spatial resolution | Temporal resolution when applicable | Data format | Sample data description in the text |
|---|---|---|---|---|
| **Total fossil fuel, ocean, and land fluxes** | Global | Annual | *csv* | Figure 4 (section 4.1) |
| **Climatology mean NBE, variability, and uncertainties** | PFT and continents based 28 regions | N/A | *csv* | Figure 5 (section 4.2) |
| | Geographic-based 13 regions | | *csv* | |
| | TransCom regions | | *csv* | |
| **Hemispheric NBE and uncertainties** | NH (20°N-90°N), tropics (20°S-20°N), and SH (60°S-20°S) | Annual | *csv* | Figure 6 (section 4.3) |
| **NBE variability and uncertainties** | PFT and continents based 28 regions | Annual | *csv* | Figure 7 (section 4.3) |
| | Geographic -based 13 regions | | *csv* | |
| | TransCom regions | | *csv* | |
| **NBE seasonality and its uncertainties** | PFT and continents based 28 regions | Monthly | *csv* | Figure 8 (section 4.4) |
| | Geographic -based 13 regions | | *csv* | |
| | TransCom regions | | *csv* | |
| **Monthly NBE and uncertainties** | PFT and continents based 28 regions | Monthly | *csv* | N/A |
| | Geographic -based 13 regions | | *csv* | |
| | TransCom | | *csv* | |
| **Gridded posterior NBE, air-sea carbon exchanges, and uncertainties** | 4° (latitude) x 5° (longitude) | Monthly | *NetCDF* | N/A |
| **Gridded prior NBE and air-sea carbon exchanges** | 4° (latitude) x 5° (longitude) | Monthly and 3-hourly | *NetCDF* | N/A |
| **Gridded fossil fuel emissions** | 4° (latitude) x 5° (longitude) | Monthly mean and hourly | *NetCDF* | N/A |
| **Region masks** | PFT and continents based 28 regions | N/A | csv | Figure 3 (section 2.4) |
| | Geographic -based 13 regions | | | |
| | TransCom regions | | | |

1209

1210

**Table: 6 The nine-year mean regional annual fluxes, uncertainties, and variability. Regions are based on the mask shown in Figure 5A (Figure 5.csv). Unit: GtC/year**

| Region name (Figure4.csv) | Mean NBE | Uncertainty | Variability |
|---|---|---|---|
| **NA shrubland** | -0.14 | 0.02 | 0.05 |
| **NA needleleaf forest** | -0.22 | 0.04 | 0.06 |
| **NA deciduous forest** | -0.2 | 0.04 | 0.07 |
| **NA crop natural vegetation** | -0.41 | 0.06 | 0.18 |
| **NA grassland** | -0.04 | 0.03 | 0.03 |
| **NA savannah** | 0.03 | 0.02 | 0.03 |
| **Tropical South America (SA) evergreen broadleaf** | 0.04 | 0.1 | 0.28 |
| **SA savannah** | -0.09 | 0.06 | 0.18 |
| **SA cropland** | -0.07 | 0.03 | 0.07 |
| **SA shrubland** | -0.03 | 0.02 | 0.08 |
| **Eurasia shrubland savanna** | -0.44 | 0.07 | 0.14 |
| **Eurasia needleleaf forest** | -0.41 | 0.07 | 0.12 |
| **Europe cropland** | -0.46 | 0.09 | 0.16 |
| **Eurasia grassland** | 0.02 | 0.08 | 0.13 |
| **Asia cropland** | -0.37 | 0.13 | 0.08 |
| **India** | 0.14 | 0.09 | 0.14 |
| **Tropical Asia savanna** | -0.12 | 0.11 | 0.08 |
| **Tropical Asia evergreen broadleaf** | -0.09 | 0.09 | 0.12 |
| **Australia (Aus) savannah grassland** | -0.11 | 0.02 | 0.09 |
| **Aus shrubland** | -0.07 | 0.01 | 0.05 |
| **Aus cropland** | -0.01 | 0.01 | 0.03 |
| **African (Afr) northern shrubland** | 0.04 | 0.02 | 0.03 |
| **Afr grassland** | 0.03 | 0.01 | 0.01 |
| **Afr northern savanna** | 0.54 | 0.15 | 0.49 |
| **Afr southern savanna** | -0.27 | 0.18 | 0.33 |
| **Afr evergreen broadleaf** | 0.1 | 0.07 | 0.09 |
| **Afr southern shrubland** | 0.01 | 0.01 | 0.01 |
| **Afr desert** | 0.06 | 0.01 | 0.04 |

**Table: 7 Lists of data sources used in producing and evaluating posterior NBE product.**

| Data name | Data Source |
|---|---|
| ECCO-Darwin ocean fluxes | https://doi.org/10.25966/4v02-c391 |
| CARDAMOM NBE and uncertainties | https://doi.org/10.25966/4v02-c391 |
| ODIAC | http://db.cger.nies.go.jp/dataset/ODIAC/DL_odiac2019.html |
| GOSAT b7.3 | https://oco2.gesdisc.eosdis.nasa.gov/data/GOSAT_TANSO_Level2/ACOS_L2S.7.3/ |
| OCO-2 b9 | https://disc.gsfc.nasa.gov/datasets?page=1&keywords=OCO-2 |
| ObsPack | https://www.esrl.noaa.gov/gmd/ccgg/obspack/data.php |
| ATom 1-4 | https://daac.ornl.gov/ATOM/guides/ATom_merge.html |
| HIPPO 3-5 | https://www.eol.ucar.edu/field_projects/hippo |
| INPE | https://www.esrl.noaa.gov/gmd/ccgg/obspack/data.php?id=obspack_co2_1_INPE_RESTRICTED_v2.0_2018-11-13 and |
| FLUXSAT-GPP | https://gs614-avdc1-pz.gsfc.nasa.gov/pub/tmp/FluxSat_GPP/ |
| NOAA MBL reference | https://www.esrl.noaa.gov/gmd/ccgg/mbl/index.html |
| CarbonTracker-Europe NBE | https://www.carbontracker.eu/download.shtml |
| Jena CarbonScope NBE | http://www.bgc-jena.mpg.de/CarboScope/?ID=s |
| CAMS NBE | https://apps.ecmwf.int/datasets/data/cams-ghg-inversions/?date_month_slider=2009-12,2018-12&param=co2&datatype=ra&version=v17r1&frequency=mm&quantity=surface_flux |
| Posterior NBE | https://doi.org/10.25966/4v02-c391 |